nature chemical biology

ARTICLES

https://doi.org/10.1038/s41589-021-00840-4

Designer membraneless organelles sequester native factors for control of cell behavior

Mikael V. Garabedian[1], Wentao Wang[2], Jorge B. Dabdoub[1], Michelle Tong[1], Reese M. Caldwell[1], William Benman[2], Benjamin S. Schuster[3], Alexander Deiters[4] and Matthew C. Good[1,2]✉

Subcellular compartmentalization of macromolecules increases flux and prevents inhibitory interactions to control biochemical reactions. Inspired by this functionality, we sought to build designer compartments that function as hubs to regulate the flow of information through cellular control systems. We report a synthetic membraneless organelle platform to control endogenous cellular activities through sequestration and insulation of native proteins. We engineer and express a disordered protein scaffold to assemble micron-size condensates and recruit endogenous clients via genomic tagging with high-affinity dimerization motifs. By relocalizing up to 90% of targeted enzymes to synthetic condensates, we efficiently control cellular behaviors, including proliferation, division and cytoskeletal organization. Further, we demonstrate multiple strategies for controlled cargo release from condensates to switch cells between functional states. These synthetic organelles offer a powerful and generalizable approach to modularly control cell decision-making in a variety of model systems with broad applications for cellular engineering.

Cells can enhance the rate and fidelity of biochemical reactions through subcellular compartmentalization[1]. For example, membrane-bound organelles, such as the nucleus and lysosome, display highly selective partitioning of biological cargo. Their restricted permeability increases reactivity via enforced proximity and ensures specificity by insulating components from competing reactions[2–6]. Cells also contain membraneless organelle subcompartments, such as the nucleolus and P granules, that form through the self-assembly and coacervation of disordered proteins and RNA into mesoscale biomolecular condensates[7]. By harnessing principles of protein self-assembly, it is possible to construct nano- or microcompartments inside a cell that encapsulate enzymes and substrates to control or augment their functions in living systems[8–10]. One such strategy has been to assemble designer compartments that colocalize components to enhance reaction rates of exogenous pathways[11,12]. A second important strategy, the use of synthetic organelles to sequester user-defined, native proteins for control of cellular decision-making, has yet to be demonstrated.

Synthetic condensates or membraneless organelles can be assembled in a cell from the expression of disordered protein sequences above their saturation concentration. Low-complexity sequences from Fus and other Fus/EWS/TAF15 (FET) family members, reslin-like sequences and arginine/glycine-rich (RGG) domains from LAF-1 have been used to generate synthetic condensates in bacterial, yeast and mammalian systems[13–18]. We previously showed the utility of a disordered protein platform for generating condensates in vitro in synthetic cell-like compartments[18]. The 168-amino acid disordered RGG domain of the *Caenorhabditis elegans* P granule protein LAF-1 is necessary and sufficient for phase separation and does not require RNA for self-assembly[18–20]. Importantly, the valency of the RGG domain tunes the critical concentration for liquid–liquid phase separation (LLPS), and real-time reduction of valency promotes condensate disassembly. Further, enzymatic and optical release of a solubilization domain from RGG initiates condensate assembly[21,22]. In addition, transient expression in cells leads to the formation of liquid-like micron-size condensates[18].

In living cells, biomolecular condensates and membraneless organelles sequester client enzymes or RNAs to either increase enzymatic flux or to insulate them from other cellular machinery. For example, in response to various stresses, mammalian cells form stress granules to sequester proteins, RNA and elongation factors, a response that prevents stress-induced cellular senescence[23]. Guided by this insulation mechanism, we sought to develop our own synthetic membraneless organelle platform that functions to sequester and insulate native enzymes for modular control over cellular functions. For these designer organelles to have broad utility in cell biology and engineering applications, they should exhibit restricted permeability, show highly selective and efficient enrichment of specific cargoes and be capable of controllable client release. Throughout this article, we refer to our platform as synthetic organelles or condensates interchangeably.

Enforced localization of exogenously expressed clients in cells has been demonstrated using synthetic condensate systems[11,13,15,18,24]. A common strategy tags the exogenous client with the same disordered protein sequence domain present on the intrinsically disordered protein (IDP) scaffold to direct partitioning to synthetic condensates[12,15,16,18]. However, concerns arise about integrating large, disordered domains into endogenous gene loci, particularly whether they are orthogonal or may alter endogenous protein functionality. Further, it is not clear whether this IDP-tagging approach is generalizable and capable of sequestering a majority of the endogenously expressed target protein in the cell. Therefore, a substantial advance would be the development of a synthetic condensate platform in which a majority of the scaffold protein partitions to the condensate to achieve high fractional client recruitment. Combined with a modular strategy for localizing clients without disrupting their native function, for example, using coiled-coil interaction motifs, a key capability would be functional insulation of native enzymes. An

[1]Department of Cell and Developmental Biology, University of Pennsylvania, Philadelphia, PA, USA. [2]Department of Bioengineering, University of Pennsylvania, Philadelphia, PA, USA. [3]Department of Chemical and Biochemical Engineering, Rutgers University, Piscataway, NJ, USA. [4]Department of Chemistry, University of Pittsburgh, Pittsburgh, PA, USA. ✉e-mail: mattgood@pennmedicine.upenn.edu

additional engineering demand is reversibility of client recruitment, enabling controlled release from a designer organelle to restore pathway function and switch cells between functional states.

In this study, we developed such a synthetic membraneless organelle system to insulate and functionally knockdown essential native enzymes via compartmentalization and achieve modular control of cellular behavior. We demonstrate successful engineering of a number of platform functions; we achieve nearly full partitioning of scaffold and native clients to the synthetic organelle by screening through IDP valencies and recruitment tags. By genomic tagging of native gene loci, we show functional insulation of enzymes that regulate the cell cycle control system and actin cytoskeleton, thereby switching cells from a proliferation state to an arrested state and from polarized to isotropic cytoskeletal organization. We demonstrate the feasibility of rapid induced client recruitment and switching of cell behavior. Further, we demonstrate thermal and optical strategies for controlled release of clients localized to the synthetic organelle for reversible control of the cell activity state. Finally, we demonstrate the feasibility of implementing this platform in mammalian cells by CRISPR tagging of endogenous gene loci to efficiently partition and relocalize native enzymes. We propose that this designer membraneless organelle system, embedded with interaction tags, offers a powerful and generalizable chemical biology tool for controlling cellular activities. The applications of our approach range from real-time probing of pathways in cell biology to mesoscale protein switches for cellular engineering and synthetic biology.

Results

Targeting clients to synthetic membraneless organelles. Our first goal was to augment living cells with synthetic compartments, screening them for temperature stability and critical concentration to achieve a high fraction of IDP scaffold in condensates. Constructs containing a single RGG domain have poor LLPS activity in vivo, consistent with previous in vitro findings (Extended Data Fig. 1a–c)[18]. Addition of a second RGG domain allowed condensate formation at 25 °C, but was not stable at higher temperatures (Extended Data Fig. 1a,c). A scaffold encoding three RGG domains, however, allowed for robust condensate formation and stability over a wide range of temperatures (Extended Data Fig. 1a–c). Importantly, these in vivo structures maintained liquid-like features (Extended Data Fig. 1d,e).

Our second goal was to test various protein interaction motifs for tagging clients to stably or reversibly enforce their proximity to our synthetic organelle (Fig. 1a). We encoded cognate interaction motifs on the N terminus of the IDP scaffold protein and C terminus of client proteins. Our testing set included (1) short coiled-coil SYNZIP pairs (SZ1, SZ2), (2) thermally reversible coiled-coil domains, TsCC(A) and TsCC(B), which are shortened forms of a bacterial thermometer (TlpA) engineered to form heterodimers[25] whose DNA-binding domain has been removed, and (3) small molecule-inducible dimerization domains FRB and FKBP (Fig. 1b).

Next, we determined the in vivo phase boundaries for the various RGG scaffolds and characterized the number and size of condensates per cell. When fused to an N-terminal SZ1 coiled, the $(RGG)_3$–GFP scaffold formed an average of five condensates per cell (Fig. 1c,d). Addition of the TsCC(A) domain to $(RGG)_3$-GFP scaffolds led to fusion and formation of one to two large condensates per cell (Fig. 1c,d). To better evaluate the phase behavior of these condensates in vivo, we measured the intracellular phase boundaries for scaffolds containing various RGG domains and tags (Fig. 1e). An SZ1–$(RGG)_2$–GFP scaffold protein had a saturation concentration (C_{sat}) of approximately 1,610 nM. Addition of a third RGG domain lowered the C_{sat} to ~600 nM, in agreement with previous in vitro findings[18]. The TsCC(A)–$(RGG)_3$–GFP scaffold demonstrated an even larger reduction of C_{sat} to ~29 nM, likely due to some coiled-coil homodimerization activity (Fig. 1e and Extended Data Fig. 1f).

The steady-state fraction of scaffold protein that will partition to the condensate versus remain in the cytosol is determined by the C_{sat} and protein expression levels. This parameter is essential because it may impact the fraction of client recruited via cognate interaction motifs. We measured the fraction of total scaffold and client-integrated intensity present in cells after inducing scaffold expression. We found that over 95% of total TsCC(A)–$(RGG)_3$–GFP scaffold protein and approximately 72% of total SZ1–$(RGG)_3$–GFP scaffold protein localized to condensates (Fig. 1f and Extended Data Fig. 1g). Importantly, while an exogenously expressed mScarlet client fused to an interaction motif is diffusely localized through the cell (Extended Data Fig. 1h), expression of a scaffold with the cognate protein interaction motif results in robust localization of mScarlet to our synthetic condensates. Over 91% of the client tagged with TsCC(B) was recruited to TsCC(A)–$(RGG)_3$–GFP condensates (Fig. 1g), demonstrating sequestration of a vast majority of a client protein in cells at room temperature under normal growth conditions.

We also tested the feasibility of induced cargo recruitment. Our rationale was to allow a tagged client to localize and function normally in the presence of synthetic condensates under basal conditions and then rapidly induce dimerization and sequestration to the synthetic condensates. We fused FRB to the scaffold and FKBP to a client. In the absence of dimerizer, the tagged client diffused freely throughout the cytosol (Extended Data Fig. 1h), and upon the addition of rapamycin (Rap), the client was quickly relocalized to the condensates (Extended Data Fig. 1i and Supplementary Video 1). We found that this strategy could partition approximately 50% of cargo with a time for half maximal recruitment of ~12 min (Extended Data Fig. 1j).

Collectively, we achieved both stable and inducible client recruitment to our synthetic condensates and found that the TsCC(A)–$(RGG)_3$–GFP scaffold was capable of recruiting over 90% of a client tagged with the cognate interaction motif. Based on these results, we proceeded with the TsCC(A)–$(RGG)_3$–GFP scaffold for sequestering native enzymes to control cell behaviors.

Control of cell behavior by sequestering native enzymes. We tested the utility of our synthetic membraneless organelle platform as a protein-based switch to regulate cell decision-making. To modulate both sides of the cell proliferation control system, we chose as targets for sequestration the guanine nucleotide exchange factor (GEF) Cdc24 and the kinase Cdc5 (Fig. 2a). Knockout or depletion of Cdc24 prevents polarized growth and proliferation, and loss of Cdc5 prevents cells from undergoing cell division[26–29]. Our hypothesis was that by tagging these proteins with coiled coils at their genomic loci, we would sequester a sufficient fraction of the endogenous enzyme to our designer condensates, functionally insulating them and preventing pathway activity (Fig. 2b).

Tagging with a fluorophore and the TsCC(B) coiled coil does not affect the normal localization of Cdc24 to polarity sites like the yeast bud neck and tip or that of Cdc5 at spindle pole bodies[30,31] (Extended Data Fig. 2a,b). Natively expressed Cdc24–mScarlet–TsCC(B) is strongly recruited to condensates formed from TsCC(A)–$(RGG)_3$–GFP expression (Fig. 2c and Extended Data Fig. 2c), but is not recruited to control scaffolds that lack the cognate coiled-coil tag (Extended Data Fig. 2d). Enforced localization of Cdc24–mScarlet–TsCC(B) to the synthetic condensates competes it away from its native localization sites (Extended Data Fig. 2e), and this relocalization can be observed in real time following induced expression of the scaffold (Extended Data Fig. 2f and Supplementary Video 2). Importantly, both tagged Cdc24 and tagged Cdc5 are efficiently recruited (Fig. 2c,d), demonstrating that greater than 86% and 83% of the native enzymes, respectively, can be sequestered within condensates.

The behavior of cells containing endogenously tagged clients is dramatically altered by the expression of synthetic condensates functionalized with cognate recruitment tags. Cells containing

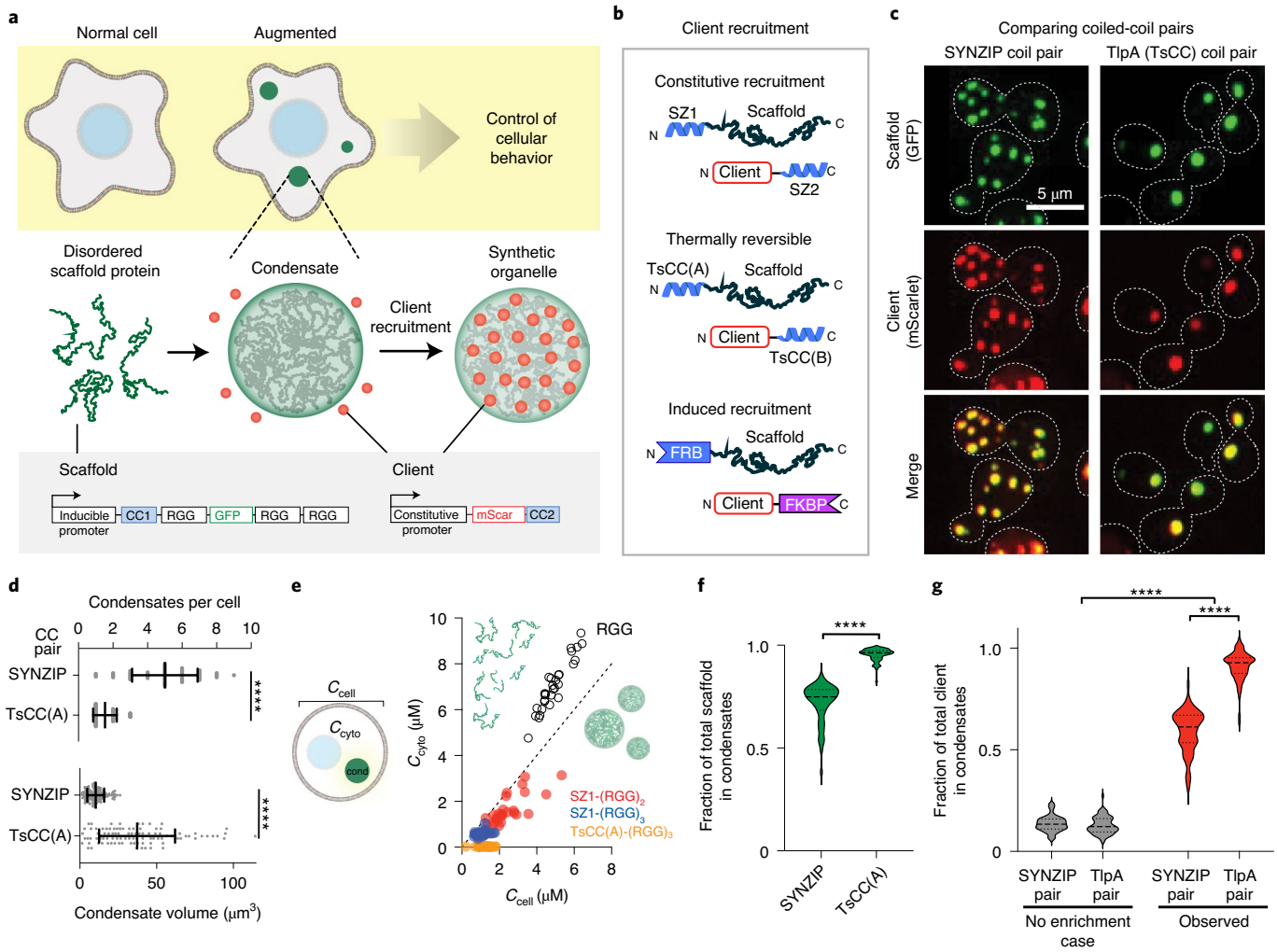

Fig. 1 | Robust cargo recruitment to synthetic condensates via protein–protein interaction domains. a, Schematic overview of assembling synthetic organelles from disordered scaffold proteins to target clients and predictably modulate cellular functions; scaffold, triple RGG, green fluorescent protein (GFP) tag and a high-affinity coiled-coil (CC) tag under the control of an inducible promoter; client, fluorophore with a cognate CC under the control of a constitutive promoter. **b**, Client recruitment strategies included SYNZIPs, thermally responsive coiled coils and rapamycin-induced dimerization domains. **c**, Representative images of a yeast cell expressing a scaffold and client with cognate SYNZIP (left) or thermally responsive (right) CC pairs. Merged images show strong recruitment of client to condensates. **d**, Comparison of mean condensate number (top) and volume (bottom) for each scaffold type; $n = 60$ cells for SYNZIP and $n = 75$ cells for TsCC(A) scaffolds. Error bars represent s.d. Significance was calculated by unpaired, two-tailed *t*-test; $^{****}P < 0.0001$. **e**, Steady-state cytoplasmic concentration of scaffold outside of condensates (C_{cyto}) as a function of total cellular concentration (C_{cell}) for 30 cells per scaffold type. The dashed line represents a slope of 1; cond, condensate. **f**, Violin plots of the fraction of total scaffold protein present in condensates for cells as in **d**. Significance was calculated by unpaired, two-tailed *t*-test; $^{****}P < 0.0001$. **g**, Violin plots of the fraction of total client recruitment to condensates with each CC pair compared to expected percentage for condensates of the same size without recruitment in cells as in **d**. Significance was calculated by one-way analysis of variance (ANOVA); $^{****}P < 0.0001$.

tagged Cdc24 or Cdc5 grow and proliferate normally in the absence of TsCC(A)–$(RGG)_3$–GFP condensates. However, their cell cycle control systems are blocked following the formation of condensates. Cdc24–mScarlet–TsCC(B) cells can no longer polarize or bud (Fig. 2e). Thus, localization of Cdc24 to condensates arrests cells (Fig. 2f and Extended Data Fig. 2g,h), leading to a nearly 12-fold drop in the rate of cell proliferation in liquid culture (Fig. 2g and Extended Data Fig. 2g) and causing cells to substantially expand in area (Extended Data Fig. 2i). Importantly, only cells expressing both a tagged Cdc24 and TsCC(A)–$(RGG)_3$–GFP scaffold show growth arrest; other cells behave similar to wild-type cells. Sequestration of Cdc5–mScarlet–TsCC(B) disrupts cell division, and cells remain dumbbell shaped (Fig. 2e). As a result, sequestration and functional insulation of Cdc5 also stalls cell proliferation (Extended Data Fig. 2j).

In addition to switching cell growth control, we wanted to test regulation of the spatial organization of the actin cytoskeleton by our synthetic condensates. To do this we targeted a yeast formin, Bnr1, which generates linear actin cables for intracellular trafficking and polarized cell growth[32,33]. By tagging a native, constitutively active form of Bnr1 in a cell that otherwise lacks formins, we efficiently sequestered 83% of it to TsCC(A)–$(RGG)_3$–GFP condensates[34] (Fig. 2h). This functional insulation of the formin prevented normal formation of actin cables and spatial polarization of the cytoskeleton (Fig. 2i,j).

Finally, to demonstrate rapid, inducible recruitment of a native enzyme, we tagged the endogenous locus of Cdc24 with an FKBP tag in cells containing FRB–$(RGG)_3$–GFP condensates (Fig. 3a). In the absence of dimerizer, the native enzyme localizes normally.

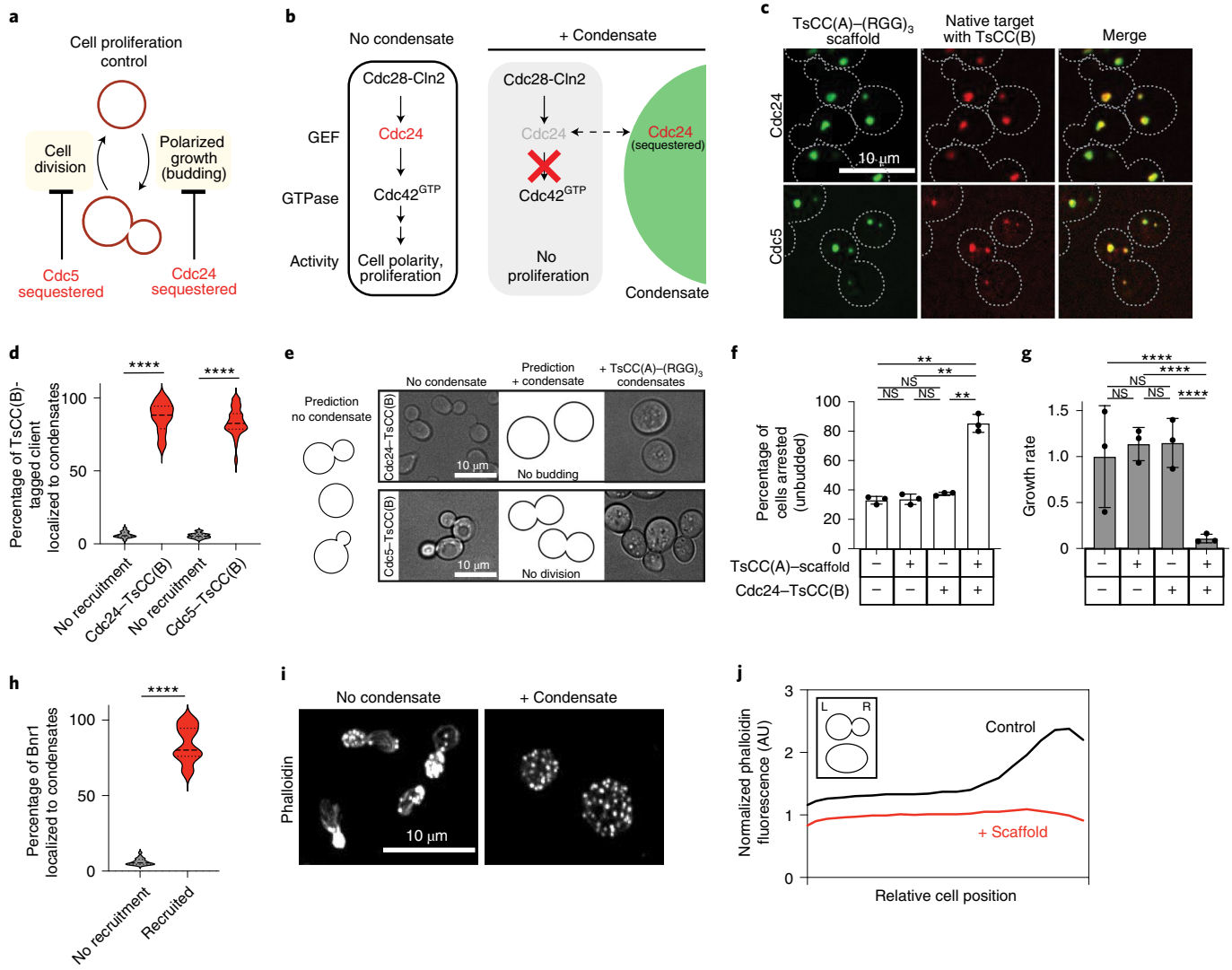

Fig. 2 | Control of cellular behavior through targeted insulation of native enzymes in synthetic organelles. a, Schematic illustration of a cell cycle control system. **b**, Illustration of hypothesis; insulation of native enzymes (e.g., Cdc24) within synthetic organelles will block their functions (e.g., signaling and cell polarization, resulting in no proliferation). **c**, Representative images of cells expressing TsCC(A)-$(RGG)_3$ scaffolds and tagged clients, showing native Cdc24–mScarlet–TsCC(B) and Cdc5–mScarlet–TsCC(B) enriched in synthetic condensates. **d**, Violin plots of the fraction of total client protein in synthetic condensates compared to the expected values for condensates with no recruitment for 50 cells per strain from 3–5 fields of view (FOVs). Significance was calculated by unpaired, two-tailed *t*-test; $^{****}P < 0.001$. **e**, Predictions and representative brightfield images of cell morphologies for tagged Cdc24 (top) and Cdc5 (bottom) before (left) and after (right) inducing scaffold expression to form condensates. **f**, Percentage of cells arrested (unbudded) in the indicated strains; $n = 150$ cells per strain pooled from three independent trials. Error bars represent s.d. Significance was calculated by one-way ANOVA (NS, not significant; $^{**}P < 0.01$). **g**, Growth rate in liquid culture for indicated strains as in **f** averaged from three independent trials. Error bars represent s.d. Significance was calculated by linear regression (NS, not significant; $^{****}P < 0.0001$). **h**, Violin plots of the fraction of total Bnr1–mScarlet–TsCC(B) in condensates compared to expected values for condensates with no recruitment; 50 cells from 305 FOVs. **i**, Representative images of phalloidin-stained Bnr1Δ*DAD*–mScarlet–TsCC(B) *bni1*Δ cells with or without condensates show altered spatial organization of the actin cytoskeleton following Bnr1 sequestration. **j**, Distribution of average phalloidin fluorescence across the cell body for 50 cells per condition from five FOVs. Cells lose polarization. The inset is a diagram of cell orientation; AU, arbitrary units; L, left; R, right.

Following the addition of Rap, Cdc24–mScarlet–FRB protein is relocalized to our synthetic condensates (Fig. 3b). Nearly 54% of the total cellular pool of tagged Cdc24 protein is sequestered to the synthetic organelle within approximately 10 min (Fig. 3c). Further, cell proliferation is effectively stalled in the presence of Rap and expressed condensates (Fig. 3d), whereas no phenotype is observed when the scaffold is expressed in the absence of dimerizer or when Rap is added to cells that lack condensates.

These results demonstrate the utility of our disordered domain-based scaffold to generate orthogonal membraneless organelles in vivo. With the addition of high-affinity coiled-coil interaction domains or inducible recruitment tags, endogenous clients are effectively sequestered and insulated in membraneless organelles. As a result, we demonstrate modular control over cell decision-making via designer compartments.

Controlled release of clients from synthetic condensates. Having demonstrated efficient functional insulation of endogenous enzymes in synthetic organelles, we next sought to develop handles for controlled intracellular release. By utilizing the thermally responsive

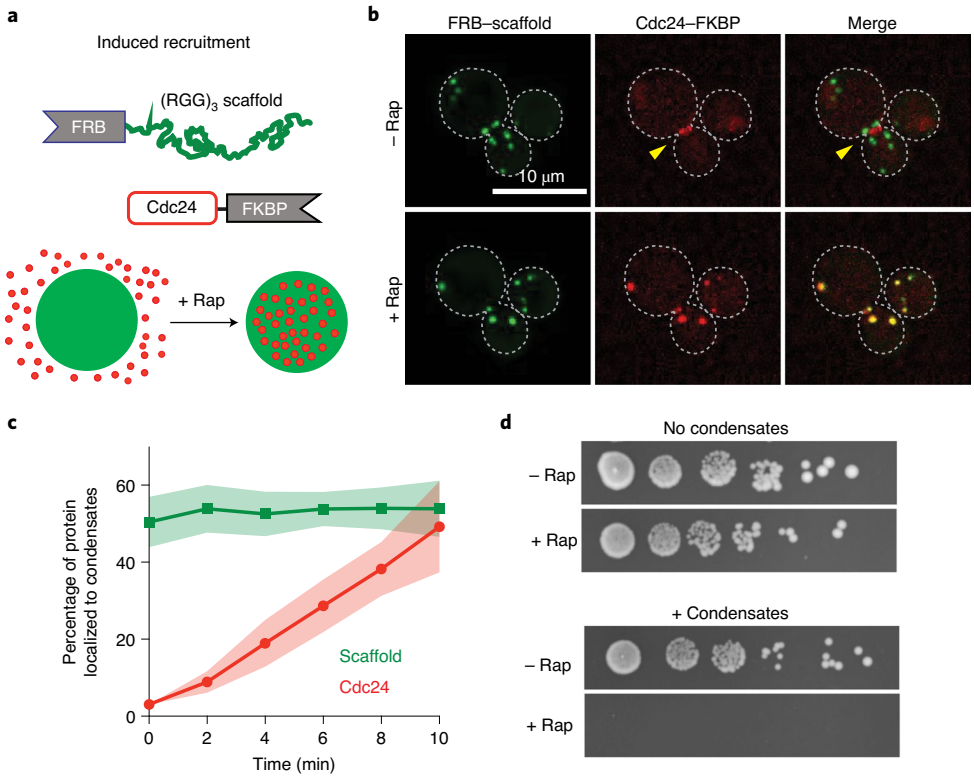

Fig. 3 | Control of cell proliferation by induced target sequestration. a, Schematic representation of rapamycin-inducible client recruitment and Cdc24–mScarlet–FKBP to FRB–$(RGG)_3$ scaffold condensates. **b**, Representative images of cells expressing Cdc24–mScarlet–FKBP and FRB–Scaffold before (top) and after (bottom) the addition of Rap. **c**, Quantification of the fraction of scaffold and client (Cdc24) in synthetic condensates over time as in **b** for 16 cells. The shaded area represents the 95% confidence interval. **d**, Spot dilution assays of the same yeast strain grown containing Cdc24–mScarlet–FKBP either lacking or expressing condensates with or without 100 nM Rap added to the medium.

TsCC(A)–TsCC(B) coiled-coil interaction pair, we hypothesized that client recruitment would be reversed above a critical temperature (Fig. 4a,b). We used Cdc24–mScarlet–TsCC(B) cells and expressed the cognate scaffold for 6 h at room temperature, during which the client was sequestered and cells were arrested, while control cells that did not express the scaffold were unresponsive (Fig. 4c). We then reversed client recruitment by raising the temperature to 37 °C or 42 °C (Fig. 4c), temperatures known to dissociate the heterodimer pair in vitro and in vivo[25]. Strikingly, we found that thermal induction successfully reversed the arrest phenotype of Cdc24–mScarlet–TsCC(B) cells expressing TsCC(A)–$(RGG)_3$–GFP condensates (Fig. 4c). This reversal was dose dependent and concomitant with a reduction of Cdc24 sequestered to the organelle (Fig. 4d); a higher temperature restored nearly wild-type levels of polarized cells. Additionally, temperature reversal of the phenotype was maintained overnight (Fig. 4c and Extended Data Fig. 3a), indicating that cells could polarize at these higher temperatures, sustaining client release.

We also sought to develop a light-based client release strategy from our synthetic organelles. Optogenetic dimerization domains have been leveraged to reverse condensate clustering or to release exogenous cargoes[11,15]. However, these strategies require sustained illumination and have not been demonstrated as effective in sequestering a large fraction of endogenous clients. We therefore decided to test an optogenetic strategy that would require short durations of illumination to achieve cargo release and reverse the programmed cell phenotype. In one strategy, we encoded a photocleavable domain, PhoCl[35,36], between the interaction tag and disordered domains of the scaffold and fluorescently tagged Cdc24 to monitor light-induced client release (Fig. 4e). We found that following short pulses of illumination, Cdc24 quickly accumulated in the cytosol (Extended Data Fig. 3b), achieving half client release from condensates in approximately 100 s (Fig. 4f). In a second strategy, we encoded a photocleavable domain, PhoCl, between the endogenous Cdc24 client and the TsCC(B) interaction tag (Extended Data Fig. 3c) and tested the functional effect of client release on switching cells between arrested and proliferative states. We initiated condensate formation to arrest the cell cycle by sequestering Cdc24 and then tested whether a pulse of illumination was sufficient to reverse the effect. We found that illumination was sufficient to stably reverse the arrest phenotype, returning cells to near-normal levels of arrest, and this was maintained for up to 6 h after light exposure (Fig. 4g). Importantly, cells containing condensates and tagged client, but lacking a photocleavable domain, did not respond to illumination (Extended Data Fig. 3d).

Finally, to determine whether it was possible to achieve cyclical control of client sequestration and release, we devised a multistep proof-of-concept experiment to cycle through cell proliferation and arrest. Scaffold expression was induced at 25 °C to first sequester client in condensates and arrest the cell cycle. In the next step, cargo was thermally released to reverse the imposed arrest, and, finally, the arrest would be reinduced by returning the temperature to 25 °C. We tested this strategy using Cdc24–mScarlet–TsCC(B) as the client and quantified cell arrest throughout the induction and release cycles. Indeed, we achieved robust arrest following organelle induction at room temperature, followed by thermal reversal of the phenotype via heating and finally restoration of the arrest by returning the system to 25 °C (Fig. 4h and Extended Data Fig. 3e,f).

Taken together, we demonstrate two distinct approaches for the release of native clients from synthetic organelles. The use of thermally responsive coiled coils enables cyclical modulation of cellular

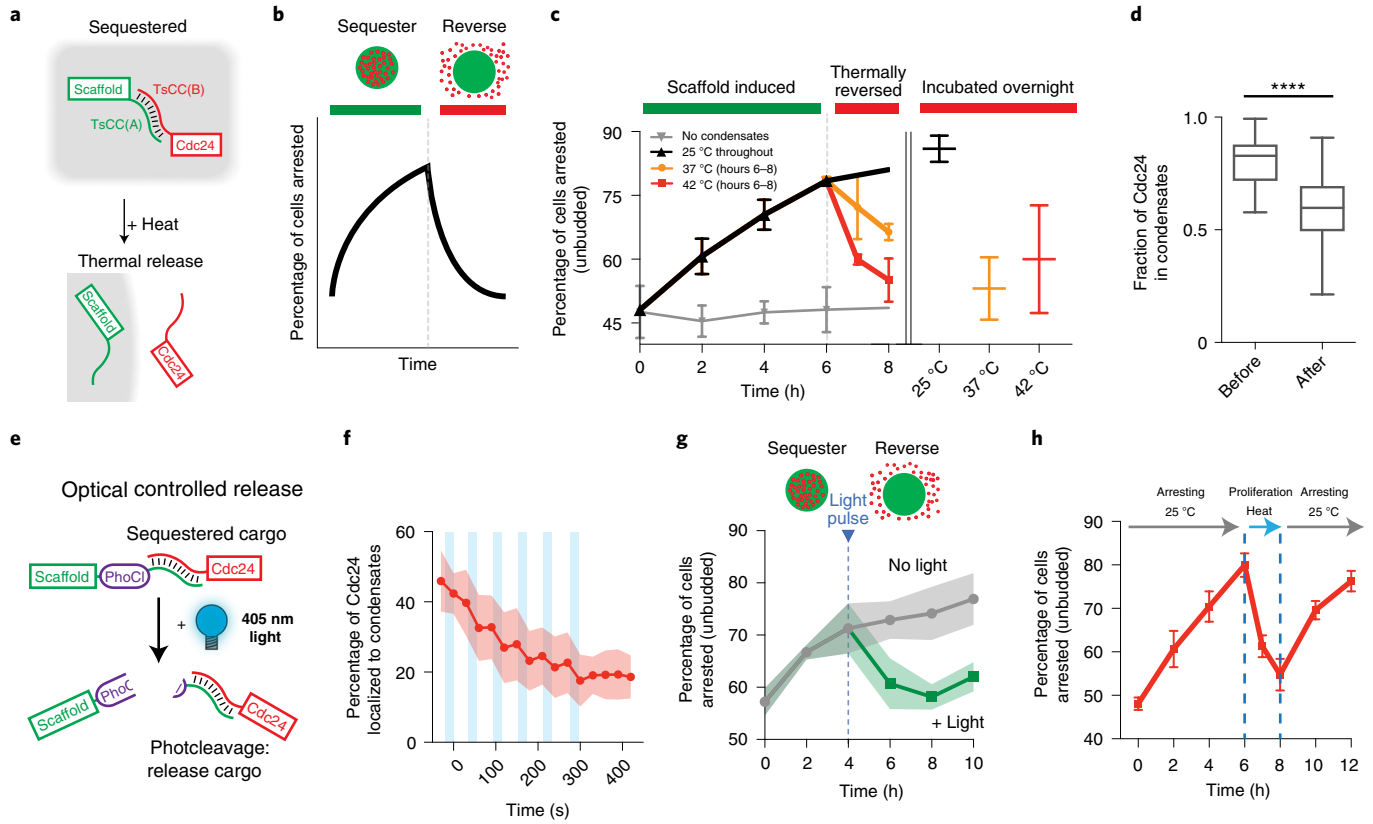

Fig. 4 | Optical and thermal client release for reversible cell cycle control. a, Schematic representation of cargo release using thermally responsive coiled coils. **b**, Schematic prediction of the switch from cell arrest to proliferation following the release of Cdc24 from synthetic condensates. **c**, Average percentage of cells arrested over time. Scaffolds were expressed at 25 °C to form synthetic condensates and induce arrest. After 6 h, cells were heated to the indicated temperatures to induce client release. Cells with no condensate expression represent the baseline (light gray). Orange and red lines represent temperature increases to 37 °C and 42 °C, respectively, for 1 and 2 h (left) and overnight (right). Cells with scaffold expression maintained at 25 °C are represented in black. Data from three trials are derived from $n = 4{,}369$ cells. Error bars represent s.d. **d**, Quantification of the fraction of Cdc24 in condensates before and after heating; $n = 10$ cells. **e**, Schematic representation of light-induced release of Cdc24 from condensates via PhoCl photocleavage on the scaffold. **f**, Quantification of the loss of Cdc24–mScarlet–TsCC(B) signal from condensates after short pulses of illumination (light blue bars, 10 s each); $n = 11$ cells. **g**, Percentage of cells arrested over time after inducing synthetic condensate expression comparing no illumination to 10 min of ultraviolet (UV) light exposure at a 4-h time point; $n = 4{,}928$ cells pooled from three trials. The shaded area represents the s.d. **h**, Cycling cells between arrest, proliferation and arrest; 25 °C from 0 to 6 h, scaffold is expressed; 42 °C from 6 to 8 h, client is released and arrest is reversed; 25 °C from 8 to 12 h, client is rerecruited and arrest is reimposed. Data are averaged from three trials and a total of 4,988 cells. Error bars represent s.d.

control systems through client sequestration–release–sequestration and an optogenetic approach for irreversible client release from condensates, which requires only a short period of illumination to stably reverse the imposed cell phenotype.

Sequestrating CRISPR-tagged targets in mammalian cells. In addition to single-cell organisms with industrial applications, we wanted to determine whether our platform to sequester native enzymes within synthetic membraneless organelles is generalizable in mammalian cells. We used a CRISPR knock-in approach to tag the 3′ end of genomic loci in U2OS cells (Extended Data Fig. 4a,b) so that clients are expressed from their endogenous promoters. We selected the GTPase Rac1 and the kinase ERK1, which have central roles in the control of cell signaling pathways regulating cell motility and proliferation[37]. In migrating cells, Rac1 activity is required at the leading edge, and in proliferating cells, Erk1 is required to transmit mitogen signals from surface receptors to downstream transcriptional effectors. Cells harboring mCherry–TsCC(B)-tagged Rac1 and ERK1 showed largely diffuse red localization throughout the cytosol, which were not recruited to condensates that lacked the correct interaction motif (Fig. 5a and Extended Data Fig. 4c). By contrast, when scaffold containing the cognate TsCC(A) tag was expressed, clients robustly localized to condensates and showed substantial enrichment in the organelles relative to the cytosol (Fig. 5a,b). Quantitation of the fraction of enzyme protein partitioned to the condensates revealed that, on average, over 70% of the scaffold protein and nearly 50% of each endogenous tagged client were localized to our synthetic organelle (Fig. 5c). To determine whether client sequestration impacts native pathway organization, we tagged the polarity protein Par6, which is normally enriched on the plasma membrane. After expressing synthetic condensates, Par6 was de-enriched from its native sites of localization and was sequestered within the condensates (Fig. 5d,e and Extended Data Fig. 4d,e).

Taken together, these data demonstrate the utility of our synthetic membraneless organelle system for modular control of essential proteins and activities in multiple cell types. By combining the expression of a designed scaffold and tagging an endogenous genomic locus with high-affinity coiled-coil interaction motifs, it is feasible to impose cell behavioral states in real time through functional sequestration of enzymes to designer membraneless compartments in cells.

Discussion

Protein engineers have only recently begun to target the self-assembly of polypeptides into mesoscale membraneless compartments

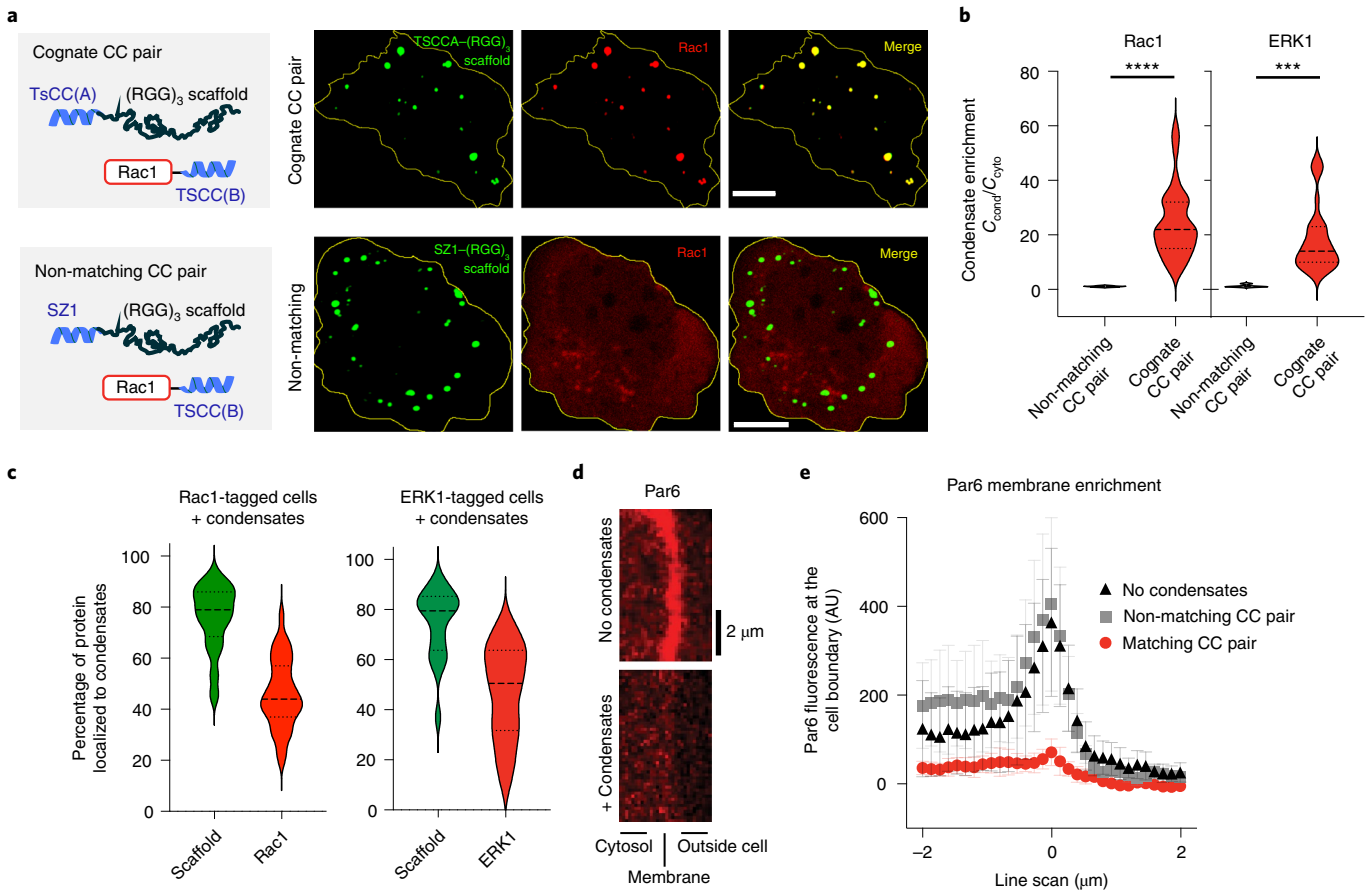

Fig. 5 | CRISPR-tagged endogenous clients enrich within synthetic condensates expressed in mammalian cells. a, Representative images of Rac1–mCherry–TsCC(B) localization in U2OS cells expressing $(RGG)_3$ scaffold with the cognate (TsCC(A)) or non-matching (SZ1) coiled coil; scale bars, 10 μm. **b**, Violin plots of client enrichment for Rac1–mCherry–TsCC(B) and ERK1–mCherry–TsCC(B) in the presence of synthetic condensates with matching and non-matching coiled coils. **c**, Percentage of scaffold and indicated endogenously tagged protein in condensates. For **b** and **c**, $n = 65$ and 20 cells pooled from four and three independent experiments for Rac1 and ERK1, respectively. **d**, Representative images of Par6–mCherry–TsCC(B) localization at the plasma membrane with no scaffold expression (top) and with scaffold expression and condensate formation (bottom). **e**, Average of line scans of Par6 at the cell boundary for cells without scaffold expression, with non-matching scaffolds and with scaffolds with cognate coiled coils; $n = 10$ cells for each line scan. Error bars represent s.d.

expressed in living cells[13,17,38]. Concurrently, metabolic engineers have leveraged these and other compartments to cluster exogenous enzymes to produce novel products[11,12]. Cellular engineers interested in programming cellular behaviors and decision-making have embedded new molecules into cells that function as receptors or switches to augment or redirect native behaviors[39–44]. Here, we expand the toolkit for cellular engineering by constructing a designer membraneless organelle system from disordered proteins that is capable of efficient client sequestration and release. When recruited to synthetic condensates, a targeted client is insulated from its native pathway, thereby generating predictable switching of cell behavior. Additionally, we demonstrate controlled release of sequestered clients from synthetic organelles using optical and thermal induction, which complement existing strategies such as light-regulated condensate disassembly. The platform is generalizable to control of a variety of native components and pathways, and we demonstrate its application in multiple cell types, including cells used for bioproduction and for mammalian tissue culture.

Cells enhance pathway flux and selectivity by enforcing the proximity of pathway components. This can be achieved by binding the components to platforms, such as macromolecular scaffold proteins, or by anchoring them to the plasma membrane[1,45]. Colocalization increases the effective concentration of proteins and reduces interactions with other competing factors in the cells. Additionally, cells achieve even higher levels of specificity through physical compartmentalization, trafficking components into membrane-bound organelles such as the nucleus or lysosome. Although these are attractive strategies for reengineering subcellular reaction schemes, they have a number of drawbacks. It is currently not feasible to rewire native lipid metabolism to create a new orthogonal compartment bounded by a lipid membrane. Also, although assembly of enzymes and substrates onto a single nanometer-size macromolecular scaffold protein can enhance flux, this reaction scheme is quite sensitive to scaffold protein concentrations and titration effects, and, thus, fluctuations in protein levels may lower reaction efficiency. Protein-based compartments offer a number of potential solutions to these engineering challenges.

Construction of synthetic subcompartments inside a cell from protein-based materials relies on polypeptides that assemble into nanocapsules or mesoscale condensates. At the nanoscale, exogenous assemblies of encapsulins or designer protein cages provide one avenue for targeting components[46–48]. However, these compartments are tens of nanometers in diameter, limiting their cargo capacity. Further, their highly restrictive permeability often prevents the diffusion of macromolecules in and out. At the microscale, multivalent binding proteins can undergo complex coacervation[10,38,49],

or disordered polypeptide polymers can self-assemble to form mesoscale condensates[7]. Native membraneless organelles, such as P granules and the nucleolus, contain disordered protein components that condense and contribute to proteinaceous compartment self-assembly[19,50]. These dynamic liquid-like compartments demonstrate selective composition and restricted permeability but are also highly porous to molecular and macromolecular clients[18]. An important feature of designer protein condensates is that they can achieve large sizes and therefore offer high payload capacities. Additionally, the dimensions and permeability of protein condensates are tunable, for example, by increasing protein polypeptide length or expression levels above the saturation concentration. Therefore, membraneless organelles provide a means to scale the output of reactions localized to the compartment, something that is harder to achieve via endogenous membrane-bound organelles.

Disordered protein sequences have been leveraged to generate synthetic liquid-like condensates in living systems. Examples in model eukaryotic culture systems include Corelets, OptoDroplets, REPS and SPLIT among others[12–14,18,21]. More recently, resilin-like polypeptide sequences have been redesigned to assemble designer condensates in prokaryotic systems[17,51]. In this work, we leveraged a disordered RGG domain from Laf-1, whose sequence displays upper critical solution temperature behavior, and phase separation can be tuned by sequence mutation or by controlling domain valency[18,20] and is amenable to engineering cytosolic condensates. We optimized the C_{sat} by changing RGG polymer valency and through interaction motifs to generate a robust condensate system that partitions more than 90% of the cellular pool of scaffold to the synthetic organelle in budding yeast. Many phase-separating proteins, including those of the FET family, possess RNA-binding RGG domains, which have been shown to enhance LLPS alone and in the presence of RNA[52]. Although we cannot exclude the idea that our RGG platform may still interact with RNAs, it does not require RNA to phase separate in biochemical reconstitution experiments[18,19], and the temperature-dependent phase behavior in cells matches behaviors from in vitro experiments (Extended Data Fig. 1b,c).

There are a variety of strategies to enrich clients in synthetic compartments, although there are strengths and limitations of each approach. Similar to localization motifs used in cells, short coiled-coil sequence pairs can be used to target a client protein to a disordered scaffold[53]. Alternatively, a disordered sequence can be appended directly to a protein of interest to target its partitioning to the scaffold only in the condensed state[11]. A challenge of fusing low-complexity polypeptide sequences to a native protein is that it may alter stability or endogenous interactions and functions. Because we wanted to target essential proteins at their genomic loci, we chose to use coiled-coil interaction pairs. These high-affinity tags have been shown to be functional and orthogonal in vivo in other cellular-engineering studies[25,53], and we demonstrate here that tagging of the GEF Cdc24 or the kinase Cdc5 with coiled-coil interaction domains does not disrupt localization and essential activities.

Additional challenges to which our system is also subject are design considerations, including the intrinsically disordered region to folded protein ratio of the scaffold and the limitations to protein expression inherent to in vivo studies. Because we rely on coacervation to form condensates capable of sequestering high levels of native clients, the scaffold must necessarily be expressed at levels well above its C_{sat}. In yeast, *GAL1* promoters lead to high expression levels, allowing us to achieve up to 90% client partitioning and control over cell behavior. However, in our transient transfections of mammalian cells, we do not achieve as high a level of scaffold expression and only obtain approximately 80% scaffold partitioning to condensates. This reduced partitioning relative to expression in yeast helps explain by we achieve lower client partitioning in mammalian cells. Future work that enhances scaffold expression, for example, via multicopy viral integration, would ensure higher fractional client partitioning. Nevertheless, using the current iteration of our platform transiently expressed in mammalian cells, we were able to recruit substantial amounts of native enzymes Rac1 and ERK1 and sequestered Par6, insulating it from its normal localization along the cell cortex.

Further, one must also consider that client size, subcellular localization and stoichiometry relative to the disordered sequences of the scaffold may affect the levels of client partitioning. We demonstrate efficient functional insulation of the GTPase Cdc24 and kinase Cdc5. Efficacy is likely high because the substrates of these enzymes are dozens of kilodaltons and therefore do not easily diffuse inside the condensates. Additionally, the normal subcellular positioning of Cdc24 to the plasma membrane and Cdc5 to spindle pole bodies likely enhances the functional effect of sequestration on shutting down pathway activity. It may be more challenging to insulate metabolic enzymes whose reactants and products are small molecules that more readily diffuse in and out of synthetic condensates. One additional unknown is whether client sequestration to synthetic condensates will exhibit an inverse size dependence at some critical size. In our current study, we effectively sequestered clients whose molecular weight is greater than 100 kDa of folded domains when including recruitment tags and fluorophores.

Our system is ostensibly similar to other inducible sequestration or inducible knockdown systems. The anchors-away approach leverages small molecule-dependent protein dimerization to anchor targets, such as transcription, outside of the nucleus[54]. However, these systems are often less effective for achieving functional knockdown of highly expressed cytoplasmic proteins, and anchoring targets to native structures, such as the plasma membrane, endoplasmic reticulum or Golgi membranes, may interfere with function. Additionally, achieving reversibility of these systems by small molecular washout is challenging. RNA interference (RNAi) strategies, although useful, can be incomplete and quite slow, taking days to sufficiently clear preexisting transcripts. Auxin-induced degradation systems overcome the time limitations of RNAi, enabling knockdown of protein levels within tens of minutes to hours[55]. However, these systems are difficult to reverse, often requiring extensive washing out of the small molecule and multiple rounds of cell division to restore protein levels. We propose that the synthetic membraneless organelle system we developed has a number of advantages. It is orthogonal, offers a high payload capacity, is capable of ultrahigh sequestration of targeted clients and demonstrates controlled client release, readily reversing the cell activity state.

Unique features of our condensate platform include regulatory handles for thermal and optical control of client release. Using thermally responsive coiled coils as interaction motifs, reversal of client recruitment to synthetic condensates can be achieved by transient shifts to elevated temperatures of 37–42 °C. Although yeast can grow normally at 37 °C, maintaining temperatures as high as 42 °C for long periods of time is not advisable and will produce a heat shock stress response. Additionally, although temperature transients are possible through ultrasound heating of mammalian cells, we would largely recommend thermal client release only for yeast. However, light-based client release is highly effective in both yeast and mammalian cells and has a number of clear applications for cell biology and cellular engineering. A simple experimental setup would be to express our disordered scaffold along with an exogenous client that one would like to release for the regulation of cellular behavior or cell fate and to illuminate the system to achieve sustained client release on the timescale of minutes. For example, sequestered signaling enzymes or transcription factors could be rapidly released to modulate a cellular decision. In effect, this system can be considered an intracellular drug delivery or controlled-release platform, one in which the kinetics of client accumulation in the cytoplasm would be substantially faster than inducible transcription and translation

In conclusion, we offer a new strategy for the programmed control of cellular decision-making by modular targeting of cellular machinery to synthetic membraneless compartments. As a proof of concept, we demonstrate near complete targeting and insulation of endogenously expressed enzymes following organelle induction. Sequestration to our designer organelles blocks its native localization and function, thereby switching off cell polarity and proliferation control systems in a single-cell system with industrial applications. Using thermosensitive interaction motifs or photocleavable domains, we show effective and cyclical reversal of client recruitment and subsequent reversal of cellular phenotypes. Further, we extend this platform to mammalian cells and show efficient client recruitment and insulation from native targeting sites, demonstrating our membraneless organelle system as generalizable across cell types and applications. Our study reveals that de novo compartmentalization of native enzymes can be used to engineer cellular systems capable of responding to specific stimuli with predictable outcomes. This synthetic organelle approach can be leveraged as a hub to insulate and rewire native biochemical pathways to reveal principles of pathway organization or as a protein switch based for cellular engineering.

Online content

Any methods, additional references, Nature Research reporting summaries, source data, extended data, supplementary information, acknowledgements, peer review information; details of author contributions and competing interests; and statements of data and code availability are available at https://doi.org/10.1038/s41589-021-00840-4.

Received: 28 September 2020; Accepted: 24 June 2021;
Published online: 02 August 2021

References

1. Good, M. C., Zalatan, J. G. & Lim, W. A. Scaffold proteins: hubs for controlling the flow of cellular information. *Science* **332**, 680–686 (2011).
2. al-Mohanna, F. A., Caddy, K. W. & Bolsover, S. R. The nucleus is insulated from large cytosolic calcium ion changes. *Nature* **367**, 745–750 (1994).
3. Burack, W. R. & Shaw, A. S. Signal transduction: hanging on a scaffold. *Curr. Opin. Cell Biol.* **12**, 211–216 (2000).
4. Burack, W. R., Cheng, A. M. & Shaw, A. S. Scaffolds, adaptors and linkers of TCR signaling: theory and practice. *Curr. Opin. Immunol.* **14**, 312–316 (2002).
5. Bhattacharyya, R. P., Reményi, A., Yeh, B. J. & Lim, W. A. Domains, motifs, and scaffolds: the role of modular interactions in the evolution and wiring of cell signaling circuits. *Annu. Rev. Biochem.* **75**, 655–680 (2006).
6. Scott, J. D. & Pawson, T. Cell signaling in space and time: where proteins come together and when they're apart. *Science* **326**, 1220–1224 (2009).
7. Banani, S. F., Lee, H. O., Hyman, A. A. & Rosen, M. K. Biomolecular condensates: organizers of cellular biochemistry. *Nat. Rev. Mol. Cell Biol.* **18**, 285–298 (2017).
8. Choudhary, S., Quin, M. B., Sanders, M. A., Johnson, E. T. & Schmidt-Dannert, C. Engineered protein nano-compartments for targeted enzyme localization. *PLoS ONE* **7**, e33342 (2012).
9. Dueber, J. E. et al. Synthetic protein scaffolds provide modular control over metabolic flux. *Nat. Biotechnol.* **27**, 753–759 (2009).
10. Aumiller, W. M. Jr., Pir Cakmak, F., Davis, B. W. & Keating, C. D. RNA-based coacervates as a model for membraneless organelles: formation, properties, and interfacial liposome assembly. *Langmuir* **32**, 10042–10053 (2016).
11. Zhao, E. M. et al. Light-based control of metabolic flux through assembly of synthetic organelles. *Nat. Chem. Biol.* **15**, 589–597 (2019).
12. Reinkemeier, C. D., Girona, G. E. & Lemke, E. A. Designer membraneless organelles enable codon reassignment of selected mRNAs in eukaryotes. *Science* **363**, eaaw2644 (2019).
13. Shin, Y. et al. Spatiotemporal control of intracellular phase transitions using light-activated optoDroplets. *Cell* **168**, 159–171 (2017).
14. Bracha, D. et al. Mapping local and global liquid phase behavior in living cells using photo-oligomerizable seeds. *Cell* **175**, 1467–1480 (2018).
15. Dine, E., Gil, A. A., Uribe, G., Brangwynne, C. P. & Toettcher, J. E. Protein phase separation provides long-term memory of transient spatial stimuli. *Cell Syst.* **6**, 655–663 (2018).
16. Song, D., Jo, Y., Choi, J. M. & Jung, Y. Client proximity enhancement inside cellular membrane-less compartments governed by client–compartment interactions. *Nat. Commun.* **11**, 5642 (2020).
17. Wei, S. P. et al. Formation and functionalization of membraneless compartments in *Escherichia coli*. *Nat. Chem. Biol.* **16**, 1143–1148 (2020).
18. Schuster, B. S. et al. Controllable protein phase separation and modular recruitment to form responsive membraneless organelles. *Nat. Commun.* **9**, 2985 (2018).
19. Elbaum-Garfinkle, S. et al. The disordered P granule protein LAF-1 drives phase separation into droplets with tunable viscosity and dynamics. *Proc. Natl Acad. Sci. USA* **112**, 7189–7194 (2015).
20. Schuster, B. S. et al. Identifying sequence perturbations to an intrinsically disordered protein that determine its phase-separation behavior. *Proc. Natl Acad. Sci. USA* **117**, 11421–11431 (2020).
21. Reed, E. H., Schuster, B. S., Good, M. C. & Hammer, D. A. SPLIT: stable protein coacervation using a light induced transition. *ACS Synth. Biol.* **9**, 500–507 (2020).
22. Caldwell, R. M. et al. Optochemical control of protein localization and activity within cell-like compartments. *Biochemistry* **57**, 2590–2596 (2018).
23. Cao, X., Jin, X. & Liu, B. The involvement of stress granules in aging and aging-associated diseases. *Aging Cell* **19**, e13136 (2020).
24. Banani, S. F. et al. Compositional control of phase-separated cellular bodies. *Cell* **166**, 651–663 (2016).
25. Piraner, D. I., Wu, Y. & Shapiro, M. G. Modular thermal control of protein dimerization. *ACS Synth. Biol.* **8**, 2256–2262 (2019).
26. Iida, H. & Yahara, I. Specific early-G1 blocks accompanied with stringent response in *Saccharomyces cerevisiae* lead to growth arrest in resting state similar to the G0 of higher eucaryotes. *J. Cell Biol.* **98**, 1185–1193 (1984).
27. Adams, A. E., Johnson, D. I., Longnecker, R. M., Sloat, B. F. & Pringle, J. R. CDC42 and CDC43, two additional genes involved in budding and the establishment of cell polarity in the yeast *Saccharomyces cerevisiae*. *J. Cell Biol.* **111**, 131–142 (1990).
28. Woods, B., Kuo, C. C., Wu, C. F., Zyla, T. R. & Lew, D. J. Polarity establishment requires localized activation of Cdc42. *J. Cell Biol.* **211**, 19–26 (2015).
29. Yoshida, S. et al. Polo-like kinase Cdc5 controls the local activation of Rho1 to promote cytokinesis. *Science* **313**, 108–111 (2006).
30. Toenjes, K. A., Simpson, D. & Johnson, D. I. Separate membrane targeting and anchoring domains function in the localization of the *S. cerevisiae* Cdc24p guanine nucleotide exchange factor. *Curr. Genet.* **45**, 257–264 (2004).
31. Botchkarev, V. V. Jr., Rossio, V. & Yoshida, S. The budding yeast Polo-like kinase Cdc5 is released from the nucleus during anaphase for timely mitotic exit. *Cell Cycle* **13**, 3260–3270 (2014).
32. Sagot, I., Klee, S. K. & Pellman, D. Yeast formins regulate cell polarity by controlling the assembly of actin cables. *Nat. Cell Biol.* **4**, 42–50 (2002).
33. Moseley, J. B. & Goode, B. L. The yeast actin cytoskeleton: from cellular function to biochemical mechanism. *Microbiol. Mol. Biol. Rev.* **70**, 605–645 (2006).
34. Chesarone, M., Gould, C. J., Moseley, J. B. & Goode, B. L. Displacement of formins from growing barbed ends by bud14 is critical for actin cable architecture and function. *Dev. Cell* **16**, 292–302 (2009).
35. Zhang, W. et al. Optogenetic control with a photocleavable protein, PhoCl. *Nat. Methods* **14**, 391–394 (2017).
36. Lu, X. *et al.* Photocleavable proteins that undergo fast and efficient dissociation. *Chemi. Sci.* https://doi.org/10.1039/D1SC01059J (2021).
37. Tanimura, S. & Takeda, K. ERK signalling as a regulator of cell motility. *J. Biochem.* **162**, 145–154 (2017).
38. Nakamura, H. et al. Intracellular production of hydrogels and synthetic RNA granules by multivalent molecular interactions. *Nat. Mater.* **17**, 79–89 (2018).
39. Gordley, R. M., Bugaj, L. J. & Lim, W. A. Modular engineering of cellular signaling proteins and networks. *Curr. Opin. Struct. Biol.* **39**, 106–114 (2016).
40. Gordley, R. M. et al. Engineering dynamical control of cell fate switching using synthetic phospho-regulons. *Proc. Natl Acad. Sci. USA* **113**, 13528–13533 (2016).
41. Wu, C. Y., Roybal, K. T., Puchner, E. M., Onuffer, J. & Lim, W. A. Remote control of therapeutic T cells through a small molecule-gated chimeric receptor. *Science* **350**, aab4077 (2015).
42. Toda, S., Blauch, L. R., Tang, S. K. Y., Morsut, L. & Lim, W. A. Programming self-organizing multicellular structures with synthetic cell–cell signaling. *Science* **361**, 156–162 (2018).
43. Li, Y. et al. Modular construction of mammalian gene circuits using TALE transcriptional repressors. *Nat. Chem. Biol.* **11**, 207–213 (2015).
44. Najem, J. S. et al. Assembly and characterization of biomolecular memristors consisting of ion channel-doped lipid membranes. *J. Vis. Exp.* https://doi.org/10.3791/58998 (2019).
45. Bashor, C. J., Helman, N. C., Yan, S. & Lim, W. A. Using engineered scaffold interactions to reshape MAP kinase pathway signaling dynamics. *Science* **319**, 1539–1543 (2008).

46. Lau, Y. H., Giessen, T. W., Altenburg, W. J. & Silver, P. A. Prokaryotic nanocompartments form synthetic organelles in a eukaryote. *Nat. Commun.* **9**, 1311 (2018).
47. Sigmund, F. et al. Bacterial encapsulins as orthogonal compartments for mammalian cell engineering. *Nat. Commun.* **9**, 1990 (2018).
48. Giessen, T. W. et al. Large protein organelles form a new iron sequestration system with high storage capacity. *eLife* **8**, e46070 (2019).
49. Li, P. et al. Phase transitions in the assembly of multivalent signalling proteins. *Nature* **483**, 336–340 (2012).
50. Feric, M. et al. Coexisting liquid phases underlie nucleolar subcompartments. *Cell* **165**, 1686–1697 (2016).
51. Dzuricky, M., Rogers, B. A., Shahid, A., Cremer, P. S. & Chilkoti, A. De novo engineering of intracellular condensates using artificial disordered proteins. *Nat. Chem.* **12**, 814–825 (2020).
52. Chong, P. A., Vernon, R. M. & Forman-Kay, J. D. RGG/RG motif regions in RNA binding and phase separation. *J. Mol. Biol.* **430**, 4650–4665 (2018).
53. Thompson, K. E., Bashor, C. J., Lim, W. A. & Keating, A. E. SYNZIP protein interaction toolbox: in vitro and in vivo specifications of heterospecific coiled-coil interaction domains. *ACS Synth. Biol.* **1**, 118–129 (2012).
54. Haruki, H., Nishikawa, J. & Laemmli, U. K. The anchor-away technique: rapid, conditional establishment of yeast mutant phenotypes. *Mol. Cell* **31**, 925–932 (2008).
55. Nishimura, K., Fukagawa, T., Takisawa, H., Kakimoto, T. & Kanemaki, M. An auxin-based degron system for the rapid depletion of proteins in nonplant cells. *Nat. Methods* **6**, 917–922 (2009).

Methods

Molecular biology. All plasmids were constructed using InFusion cloning (Takara Bio) and were verified by DNA sequencing. Yeast plasmids expressing RGG domain scaffolds were encoded in the integrating Yiplac211 (URA3, ampicillin resistance (Amp^R)) plasmid backbone downstream of the inducible *GAL1* promoter. *GAL1*, interaction tag, RGG and GFP sequences were generated by PCR and were cloned into the plasmid backbone between the XbaI and AgeI restriction sites. Plasmids expressing exogenous client (mScarlet) fused to a C-terminal interaction domain were encoded in the integrating Yiplac128 (LEU2, Amp^R) plasmid backbone downstream of a constitutive *MET17* promoter. PCR products encoding the *MET17* promoter sequence, mScarlet and an interaction tag were cloned into Yiplac128 between the XbaI and AgeI cut sites. To generate PCR products for yeast knock-ins, fluorophore and interaction domain sequences were cloned into pfa6a::KANMX6 or pfa6a::HIS3 plasmid backbones. PCR products of TsCC(B), mScarlet–TsCC(B) and mScarlet–FKBP were generated from the previously cloned Yiplac128 plasmids above and were cloned into the pfa6a vectors using the PacI and AscI restriction sites. To generate a plasmid to knock-in PhoCl–TsCC(B), PCR products of the PhoCl and TsCC(B) sequences were cloned into pfa6a::KANMX6 between PacI and AscI restriction sites via InFusion ligation. For mammalian cell work, plasmids encoding scaffolds with interaction domains were cloned into pcDNA vectors downstream of a cytomegalovirus (CMV) promoter. GFP and RGG domains were cloned from gene fragments codon optimized for human expression (Integrated DNA Technologies). Sequences were cloned into the pcDNA backbone sequentially between the BamHI and XbaI restriction sites. For mammalian CRISPR knock-ins, Cas9 plasmids with the appropriate guide RNA (gRNA) and donor plasmids encoding a fluorophore and coiled-coil interaction domains were generated. To construct Cas9 plasmids, the pCas9-guide (OriGene Technologies) was used as a backbone, and a 20-nucleotide sequence encoding the gRNA targeting the C-terminal end of the gene of interest was assembled using duplexed oligos and was cloned between BamHI and BsmBI restriction sites according to the manufacturer's instructions. Donor plasmids were constructed using the pUC19 donor backbone (Takara) and encoded 600–1,000-base pair (bp) homology arms along with mCherry–TsCC(B) and a nourseothricin *N*-acetyl transferase resistance (Neo^R) cassette in between the homology arms. The mCherry–TsCC(B) sequence was first cloned into a pcDNA backbone using the BamHI and XbaI cut sites. A 1,000-bp 5′ homology arm was generated by PCR from synthesized gene fragments (Integrated DNA Technologies) and was cloned upstream of the mCherry sequence using the NheI and BamHI restriction sites. The Neo^R cassette and a 600–800-bp 3′ homology arm were then amplified and fused by two-step PCR. These 5′ and 3′ sequences were then PCR amplified and cloned into pUC19 between the HindIII and SacI restriction sites. In each case, the PAM site, located in one of the homology arms, was changed to prevent persistent cleavage by Cas9.

Yeast procedures. Standard methodologies were followed for all experiments involving *Saccharomyces cerevisiae*[56,57]. In all cases, the scaffold was under the control of the galactose inducible *GAL1* promotor and was incorporated into the yeast *URA3* locus using an integrating vector (Yiplac211) cut with EcoRV and standard lithium acetate transformation. Exogenously expressed clients under the control of the *MET17* promotor were similarly integrated into the *LEU2* locus with an integrating vector (Yiplac128) after EcoRV digestion. To tag native genomic loci, PCR products of tags and drug resistance cassettes containing 40 to 50 bp of homology on either end of the C terminus of the target gene were transformed into yeast cells by lithium acetate/PEG transformation as previously described[58]. *BNI1* was deleted by replacing the open reading frame (ORF) with a *TRP1* marker. The DAD domain of Bnr1 was internally deleted by Cas9-mediated gene editing by cotransforming yeast strains with a plasmid expressing Cas9 and a gRNA targeting the DAD domain of *BNR1* and an 80-nucleotide oligo with homology to sequences upstream and downstream of the DAD domain[59]. All yeast strains used in this study are listed in Supplementary Table 1, and plasmids are listed in Supplementary Table 2.

For scaffold induction, yeast cells were first grown to saturation overnight in liquid YPD medium in a 25 °C shaking incubator. Cells were then washed three times in sterile water, diluted in YP + 2% raffinose and incubated in a 25 °C shaking incubator for 6 to 8 h. Finally, yeast cells were diluted to an optical density at 600 nm (OD_{600}) of 0.3 in YP + 2% galactose, and induction proceeded overnight in the same shaking incubator or for hours on a microscope slide to track scaffold induction and cargo recruitment in the same cells. The final OD_{600} values of cultures used for experiments were between 0.4 and 0.8 except for the strain harboring TsCC(A)–scaffold and endogenous Cdc24 or Cdc5 tagged with mScarlet–TsCC(B) as their growth arrests with scaffold induction. For client partitioning studies in the presence of scaffold, cells were incubated overnight in media containing galactose for ~14 h.

For thermal reversal experiments, yeast cells harboring TsCC(A)–scaffold and Cdc24–TsCC(B) were grown in YPD medium as above and were washed and transferred to YP + 2% raffinose overnight. Cells were then transferred into YP + 2% galactose to trigger scaffold induction. Thermal reversal was performed after 6 h of scaffold expression by transferring 1 ml of each cell culture to a heated water bath for 1 and 2 h. For overnight thermal reversion, cells were maintained at 37 °C or 42 °C. Samples were taken at the indicated time points, and cells were fixed with 4% paraformaldehyde (PFA) for 10 min (Ricca Chemical Company), centrifuged and washed three times with 1 ml of PBS and stored at 4 °C until imaging. For light-induced client release, yeast cells harboring a combination of TsCC(A)–PhoCl2f–scaffold and Cdc24–mScarlet–TsCC(B) or TsCC(A)–scaffold and Cdc24–PhoCl–TsCC(B) were grown, and scaffolds were expressed by switching to galactose, as above. After 4 h of scaffold expression, cells expressing TsCC(A)–PhoCl2f–scaffold and Cdc24–mScarlet–TsCC(B) were imaged and exposed to 10-s pulses of 405-nm light on an Olympus IX81 inverted confocal microscope (Olympus Life Science) with a Yokogawa CSU-X1 spinning disk, mercury lamp, 488- and 561-nm lasers and an iXon3 EMCCD camera (Andor) controlled by MetaMorph software (Molecular Devices). Cells expressing TsCC(A)–scaffold and Cdc24–PhoCl–TsCC(B) were induced as above, heated to 37 °C, exposed to a 10-min pulse of UV light and then allowed to continue to grow in YP + 2% galactose medium. Samples were taken at the indicated time points and fixed/stored as above until imaging.

For phalloidin staining, 1 ml of cell culture was fixed with 4% PFA for 1 h and centrifuged and washed three times in 1 ml of PBS. Fixed cells were resuspended in 49 µl of PBS plus 1 µl of AlexaFluor568-phalloidin (Invitrogen) and rotated in the dark at room temperature overnight. Before imaging, cells were centrifuged and washed twice with PBS.

Mammalian cell procedures. U2OS human osteosarcoma cells were cultured in Eagle's minimal essential medium (EMEM; Quality Biological) supplemented with 10% fetal bovine serum (Gibco), 2 mM L-glutamine (Gibco) and 10 U ml^{-1} penicillin–streptomycin (Gibco) and were maintained at 37 °C in a humidified atmosphere with 5% CO_2. Cells were split in a 1:3 ratio every 3 d, had been passaged for less than 2 months and were negative for known infection. Experiments were done with a confirmed viability of >95%, as determined by trypan blue staining (Gibco). For drug selection, cells were cultured in EMEM supplemented with 10% fetal bovine serum, 2 mM L-glutamine and 0.75 mg ml^{-1} G418 sulfate (MediaTech).

A CRISPR knock-in strategy was implemented to tag Rac1 and ERK1 at their native genomic loci. pUC19 donor plasmids (Takara Bio) were cloned harboring mCherry–TsCC(B) and a neomycin resistance cassette along with 600- to 1,000-bp homology arms as described above (Supplementary Table 2). Donor plasmids were cotransfected with Cas9 plasmids (OriGene Technologies) cloned with the two to three distinct gRNAs to target the gene of interest. Cotransfection of donor plasmids and pCas-gRNA plasmids was performed using Lipofectamine 2000 (Invitrogen) according to the manufacturer's protocol. Briefly, cells were seeded at 70% confluency in six-well flat-bottom tissue culture plates (CELLTREAT) 24 h before the transfection. On the day of transfection, 1,500 ng of donor plasmids and 500 ng of each pCas-gRNA plasmid were mixed in Opti-MEM reduced serum medium (Gibco). Lipofectamine 2000 was added at a 1:5 DNA-to-reagent ratio and incubated for 15 min before adding to the cells dropwise. Twenty-four hours after transfection, cells were trypsinzed and moved to 100-mm cell culture dishes (ThermoFisher Scientific). Cells were selected with drug for 7 d. After selection, cells were rested in medium without drug for 24 h and sorted based on mCherry expression using a BD FACSAria III cell sorter (BD Bioscience) with help from the flow cytometry core at the University of Pennsylvania. Briefly, cells were resuspended at 10×10^6 cells per ml in medium supplemented with 25 mM HEPES (Gibco). Before sorting, 1 µl of 1 µg ml^{-1} DAPI (Invitrogen) was added to the sample for live/dead staining. Cells were sorted into medium-expression and high-expression bins and were maintained for 2 weeks in complete medium until confluent. mCherry-positive cells were confirmed by fluorescence microscopy. CRISPR knock-in of tags to endogenous loci was confirmed via PCR.

For scaffold expression, postselection cells were seeded on 24-well glass-bottom plates (Greiner Bio-One) at 70% confluency. Twenty-four hours later, cells were transfected with 1,000 ng of GFP-tagged scaffold cloned into a pcDNA vector (Supplementary Table 2) using X-tremeGENE 9 DNA transfection reagent (Sigma-Aldrich) at a 1:3 DNA-to-reagent ratio according to the manufacturer's protocol. In all cases, cells imaged were first tested for mycoplasma using a MycoAlert mycoplasma detection kit (Lonza) according to the manufacturer's protocols. All of the cells reported in this study were determined to be mycoplasma free.

Microscopy. Fluorescence microscopy imaging of yeast and mammalian cells was performed on an Olympus IX81 inverted confocal microscope (Olympus Life Science) equipped with a Yokogawa CSU-X1 spinning disk, mercury lamp, 488- and 561-nm laser launches and an iXon3 EMCCD camera (Andor). Multidimensional acquisition was controlled by MetaMorph software (Molecular Devices). Samples were illuminated using a 488-nm laser and/or a 561-nm laser and were imaged through a ×100, 1.4-NA oil immersion objective. *Z* stacks were collected at a sampling depth appropriate for three-dimensional reconstitution. Brightfield transmitted light images used to assess yeast cell morphologies were also captured on a Nikon Eclipse Ti-U confocal microscope (Nikon) equipped with a Yokogawa CSU-X1 spinning disk and a Photometrics Evolve Delta EMCCD camera (Teledyne Photometrics).

To image mesoscale condensates, budding yeast in YP medium containing 2% galactose were immobilized to glass coverslips treated with concanavalin A (ConA). For chemogenic induction of client recruitment, yeast cells in the same

medium were first allowed to adhere to glass coverslips coated with ConA, and, subsequently, Rap was added to a final concentration of 20 μM.

For yeast photobleaching experiments (fluorescence recovery after photobleaching (FRAP) and fluorescence loss in photobleaching (FLIP)), a Roper iLas2 photoactivation system controlling a 405-nm laser was used. For FRAP, individual condensates were selected and photobleached, and fluorescence recovery in the bleached region was analyzed in ImageJ. For FLIP, half of a cell body was photobleached, and fluorescence loss from the condensate on the opposite half of the cell was analyzed in ImageJ. Mammalian U2OS cells were imaged 40 h after transient transfection after adhering to a 24-well glass-bottom plate (Greiner Bio-One). In all cases, *z* stacks were collected to visualize the scaffold at the 488-nm wavelength and the client at a 561-nm wavelength using a ×100, 1.4-NA oil immersion objective.

Image analysis. Analysis of condensates and clients in cells was performed in ImageJ. To quantify in vivo phase plots and determine C_{sat}, cells expressing scaffold were imaged alongside wells containing purified GFP fusion proteins to generate a standard curve for fluorescence. C_{cyto} was calculated from the average background-subtracted fluorescence intensity of cytoplasmic signal and was converted to concentration using the calibration curve. To quantify scaffold and client recruitment to synthetic condensates in yeast and U2OS cells, we segmented cells and condensates using ImageJ. Objects were masked in the *z* plane of the image stack containing the largest portion of cells. Because U2OS cells are adherent and spread, masks were generated in the 488-nm channel by automatic thresholding using the MaxEntropy algorithm in ImageJ, and the lower boundary was manually set to be threefold higher than the average cytosolic signal. The particle analysis function in ImageJ was used to segment condensates larger than a five-pixel area. Background-subtracted measurements of 488-nm and 561-nm pixel intensity for masks for the condensates and cells were used to calculate an enrichment index (background-corrected fluorescence $\text{intensity}_{\text{condensates}}/\text{intensity}_{\text{cytosol}}$). To estimate the fraction of scaffold or client partitioned to the organelles, we divided the background-subtracted integrated pixel intensity for condensate mask areas by the background-subtracted integrated pixel intensity of the cell mask ($\sum\text{intensity}_{\text{condensates}}/\sum\text{intensity}_{\text{cell}}$). Par6 signal at the cell cortex was analyzed by line scans in ImageJ using a line 30 pixels in length and thickened by 10 pixels. Line scans were then averaged, and background intensity was subtracted.

Quantification of cellular phenotypes (for example, budding indices and cell size) was performed in ImageJ using brightfield images of live cells or of fixed cells from time course experiments. Multiple FOVs were captured per experiment, and budding indices were generated by counting the fraction of cells that had a daughter cell (bud). Cell size measurements were performed by manual tracing of the outline of the mother cell to determine cell area. Distribution of AlexaFluor561-phalloidin staining was quantified by drawing a box that encompassed the entire cell body along the long axis of the cell and by plotting summed intensity as a function of position. Box position was determined by the position of the bud or location of polarized signal to the end of the mother cell. The longest cell axis was used in cases where a polarity axis could not be determined, such as in cells with sequestered Bnr1. Datasets were normalized to average mother cell fluorescence in cells that lacked condensates. The fluorescence profiles for at least 50 individual cells from each strain were rescaled by defining the back of the mother cell as 0 and the tip of polarized signal in G1 cells, or tip of the bud in other cell cycle stages, as 1.

Statistics and reproducibility. Experiments were reproducible. All statistical analyses were performed in GraphPad Prism 9. To test the significance of two categories, an unpaired two-tailed *t*-test was used. To test significance of more than two categories, a one-way ANOVA was used. To compare differences in growth curves, significance was determined by linear regression analysis. In all cases, NS indicates not significant; $^{*}P \leq 0.05$, $^{**}P \leq 0.01$, $^{***}P \leq 0.001$ and $^{****}P \leq 0.0001$.

Reporting Summary. Further information on research design is available in the Nature Research Reporting Summary linked to this article.

Data availability

All data supporting the findings of this study are included in the published article and its supplementary information files. Original data are available from the corresponding authors upon reasonable request. Source data are provided with this paper.

References

56. Sambrook, J., Fritsch, E. F. & Maniatis, T. *Molecular Cloning: A Laboratory Manual* 2nd edn (Cold Spring Harbor Laboratory, 1989).
57. Guthrie, G. C. & Fink, G. Guide to yeast genetics and molecular biology. *Methods Enzymol.* **194**, 1–863 (1991).
58. Longtine, M. S., Fares, H. & Pringle, J. R. Role of the yeast Gin4p protein kinase in septin assembly and the relationship between septin assembly and septin function. *J. Cell Biol.* **143**, 719–736 (1998).
59. Anand, R., Memisoglu, G. & Haber, J. Cas9-mediated gene editing in *Saccharomyces cerevisiae*. Preprint at *Protocol Exchange* https://doi.org/10.1038/protex.2017.021a (2017).

Acknowledgements

We thank A. Kumar for sharing yeast strains, the E. Bi lab for yeast plasmids and technical support, B. Xia and H. Ahmed for cloning, H. Ramage for U2OS cell lines, the M. Shapiro lab for TlpA plasmids, the D. Hammer lab for critical reading of the manuscript and A. Stout and the Penn CDB Microscopy Core for imaging and support. This cellular-engineering study was supported by a National Institute of Biomedical Imaging and Bioengineering R01 grant EB028320 (M.C.G.). Biochemical characterization of disordered proteins was partly funded by a National Science Foundation (NSF) iSuperseed grant DMR1720530 (M.C.G.). Synthesis of optochemical dimerizers was supported by NSF grant CHE-1404836 (A.D.). Conceptual development of condensates as decision hubs and investigator salary support was supported, in part, by a Department of Energy BES Biomolecular Materials grant DE-SC0007063 (M.C.G.).

Author contributions

M.V.G., J.B.D., W.W., R.M.C., W.B. and M.C.G. conceptualized the project and designed the experiments. J.B.D., M.T. and W.B. performed initial characterization of scaffold valency on condensate formation and client recruitment in yeast. M.V.G. performed cloning, strain generation and imaging for yeast experiments throughout the article. W.W. generated mammalian knock-in cell lines, imaged them and characterized client relocalization. B.S.S. contributed imaging data from yeast experiments included in Extended Data Fig. 1. A.D. contributed synthesized dimerizers. M.V.G., W.W. and M.C.G. analyzed data. M.V.G. and M.C.G. wrote the manuscript.

Competing interests

The authors declare no competing interests.

Additional information

Extended data is available for this paper at https://doi.org/10.1038/s41589-021-00840-4.

Supplementary information The online version contains supplementary material available at https://doi.org/10.1038/s41589-021-00840-4.

Correspondence and requests for materials should be addressed to M.C.G.

Peer review information *Nature Chemical Biology* thanks Ulrich Krauss and the other, anonymous, reviewer(s) for their contribution to the peer review of this work.

Reprints and permissions information is available at www.nature.com/reprints.

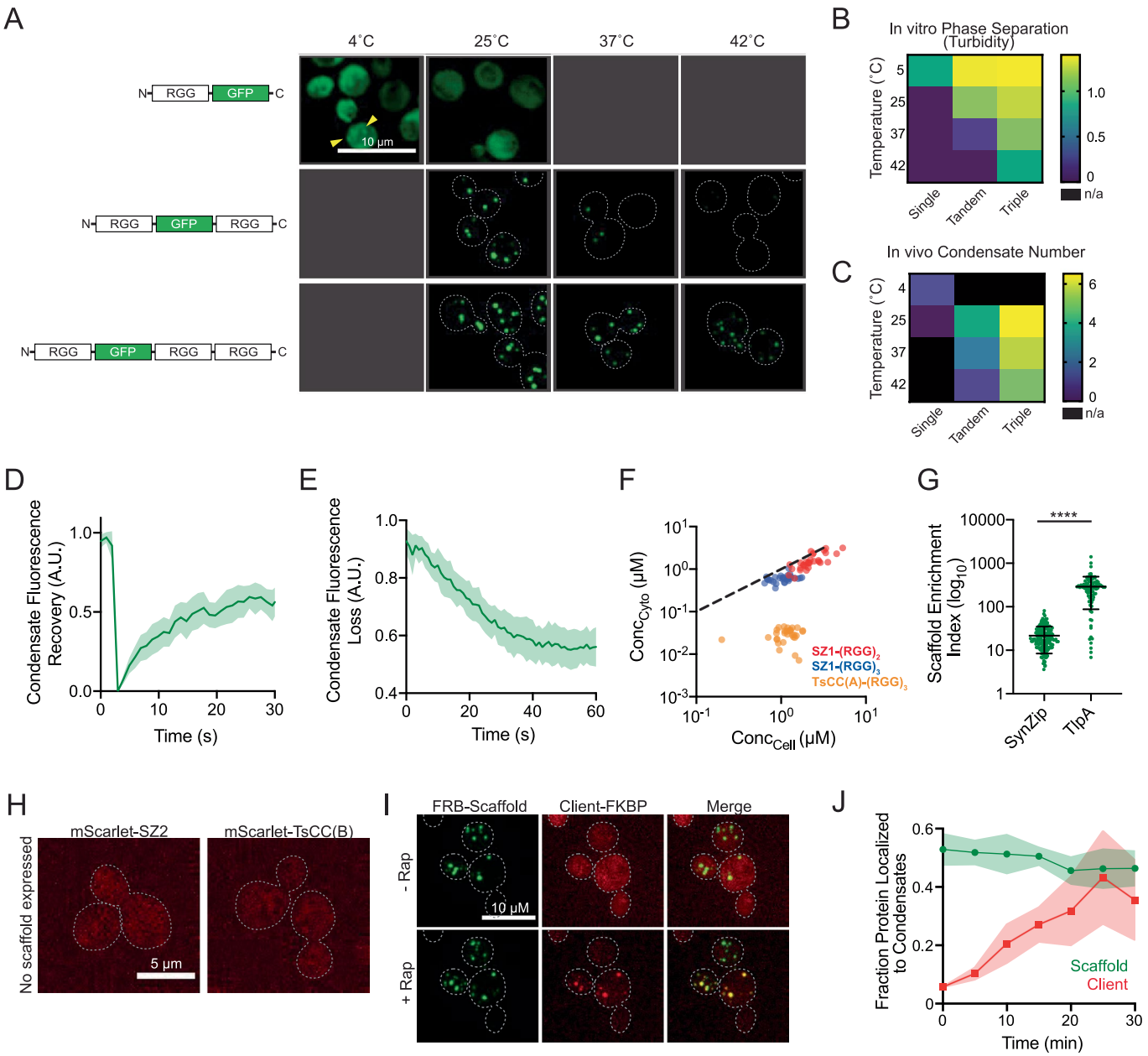

Extended Data Fig. 1 | Properties of in vivo synthetic condensates. a, Temperature dependence of condensate assembly as a function of scaffold RGG domain valency. Representative images of yeast cells expressing galactose induced GFP tagged scaffold with 1, 2, or 3 RGG domains at different temperatures. **b**, Heat map: quantitation of turbidity data of purified proteins from Schuster et al., 2018. **c**, Heat map: number of condensates per cell as a function of temperature and RGG domain valency. **d**, Fluorescence recovery after photobleaching (FRAP) of condensates formed by $(RGG)_3$ scaffold; n = 10 condensates. Shaded area, 95% CI. **e**, Fluorescence loss in photobleaching (FLIP) of condensates formed by $(RGG)_3$ scaffold. n = 13 cells. **f**, Steady state cytoplasmic scaffold concentration outside of condensates (C_{cyto}) as a function of cellular concentration (C_{cell}) for 30 cells per scaffold type. Dashed line, slope of 1. **g**, Average enrichment of scaffold protein in condensates for SZ1-$(RGG)_3$ or TsCC(A)-$(RGG)_3$. n = 164 and 97 condensates respectively. Error bars, s.d. **h**, Representative images of exogenously expressed mScarlet-SZ2 and mScarlet-TsCC(B) diffusely distributed in cytosol in the absence of condensates. **i**, Representative images of cells expressing FRB-$(RGG)_3$ scaffold and mScarlet-FKBP as a client. The client is diffuse in the cytosol before the addition of Rap and concentrated in condensates after Rap addition. **j**, Quantitation of the fraction of client protein as in i localized to condensates over time after Rap addition. n = 15 cells. Shaded area 95% CI.

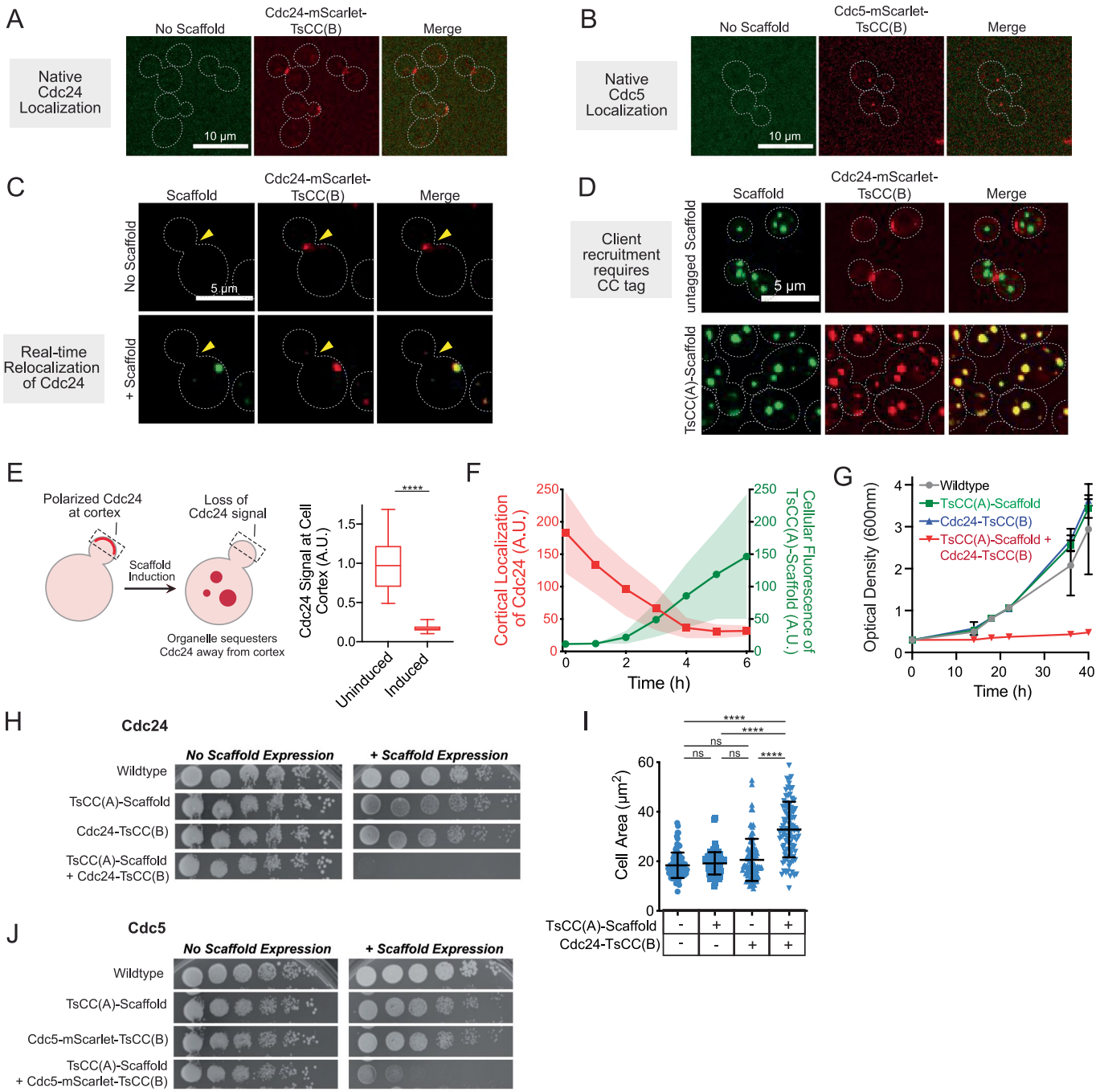

Extended Data Fig. 2 | Condensate expression relocalizes tagged native clients and regulates cell growth. a, Representative images of tagged, natively expressed Cdc24 show its cortical localization. **b**, Representative images of tagged natively expressed Cdc5 show its punctate localization to spindle pole body. **c**, Images of the same Cdc24-mScarlet-TsCC(B) cell before and after induced expression of TsCC(A)-$(RGG)_3$ scaffold for 6 hr, show loss of cortical Cdc24 signal and partitioning to synthetic condensate. **d**, Client recruitment to condensates specifically depends on CC tag interaction; Cdc24 does not interact with $(RGG)_3$ condensates that lack the interaction tag. **e**, Left, scheme: cortical Cdc24 is relocalized from cortex to synthetic condensates after induction of scaffold. Right, Average cortical Cdc24- mScarlet-TsCC(B) signal before and after TsCC(A)-$(RGG)_3$ scaffold expression (6 hr). n = 20 cells before and after hours of galactose induction. Significance calculated by unpaired, two-tailed, t-test (****, $p < 0.0001$). **f**, Kinetics of loss of cortical Cdc24-mCherry-TsCC(B) signal (red) concomitant with cellular accumulation of expressed TsCC(A)-$(RGG)_3$ scaffold (green) upon induction with galactose for 20 cells over 6 hours. Shaded area, s.d. **g**, Cell proliferation: measurements of cell density (OD600) over time for indicated Cdc24 strains in liquid media containing galactose. **h**, Growth assay for Cdc24 strains: five-fold serial dilution of indicated strains grown on solid- media containing glucose or galactose. **i**, Average cell area of mother cells only increases upon TsCC(A)-$(RGG)_3$ expression in Cdc24-mScarlet-TsCC(B) cells, consistent with cell cycle arrest in G1. **j**, Growth assay for Cdc5 strains: five-fold serial dilution of indicated strains grown on solid-media containing glucose or galactose. In all cases, growth defect depends on presence of tagged client and expression of scaffold to form condensates. Phenotype is not observed with only native client tagging or only scaffold expression.

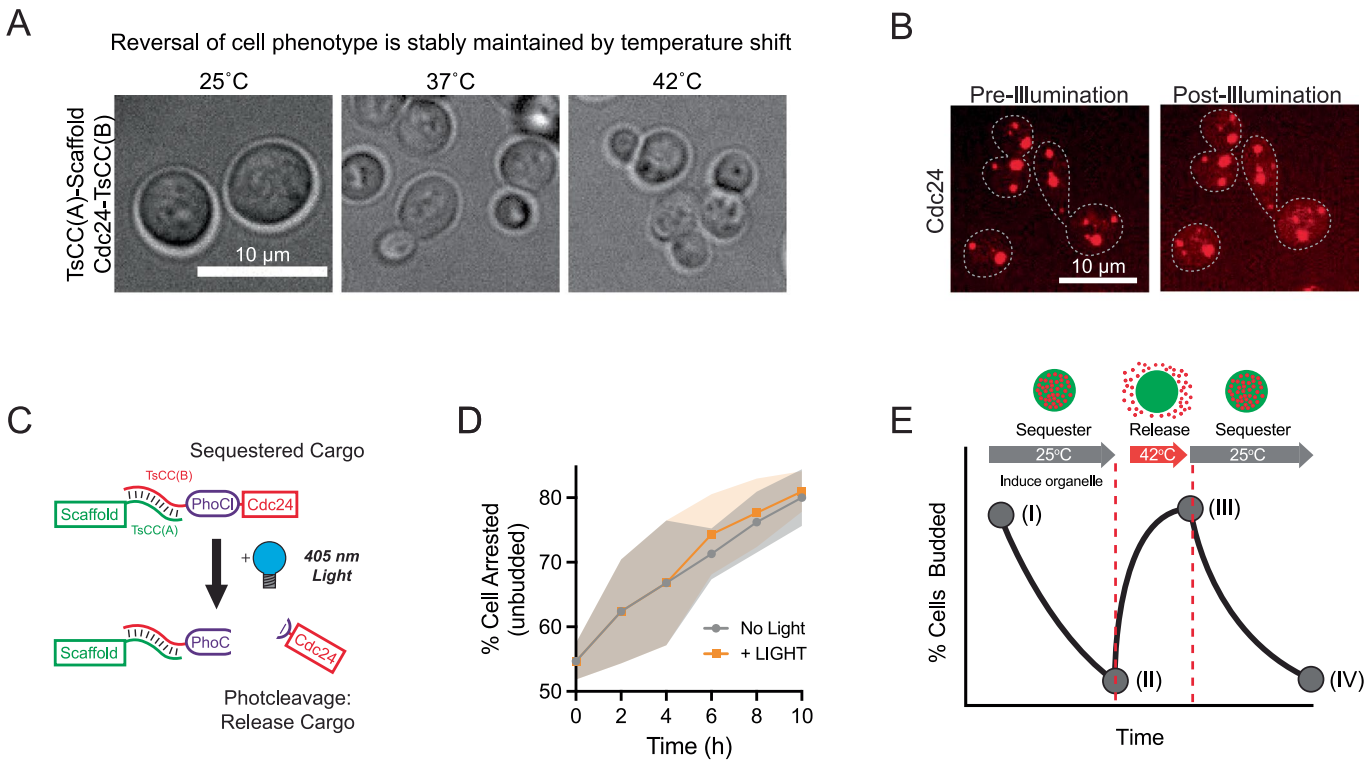

Extended Data Fig. 3 | Reversible control of cell proliferation-arrest state. a, Representative images of Cdc24-mScarlet-TsCC(B) cells expressing TsCC(A)-$(RGG)_3$ scaffold at the indicated temperatures for 14 hours. Thermally responsive coiled-coil pair dissociate upon heating to 37 or 42 °C, releasing client to promote cell polarity and reversing the cell cycle arrest associated with Cdc24 sequestration to condensates. **b**, Representative images of Cdc24-mScarlet-TsCC(B) in the presence of TsCC(A)-PhoCl2f-(RGG)3 before and after illumination with 405 nm light. **c**, Schematic of client release strategy: Cdc24 is tagged with PhoCl-TsCC(B). 405 nm light results in PhoCl cleavage and client release. **d**, Percentage of cells expressing Cdc24-mScarlet-TsCC(B) arrested (unbudded cells) over time after scaffold induction +/− illumination. n = 4048 cells in total pooled from three trials. **e**, Prediction: cycling of cell state between budded-arrested-budded-arrested. **f**, Representative images of cells at the indicated time points. Wildtype levels of budding at time 0 h. Cells incubated in galactose at 25 °C from 0-6 h timepoints to induce condensate formation, blocking budding, then heated from 6 h to 8 h timepoints, promoting polarization and budding and cooled back to 25 °C and arrested by 12 h.

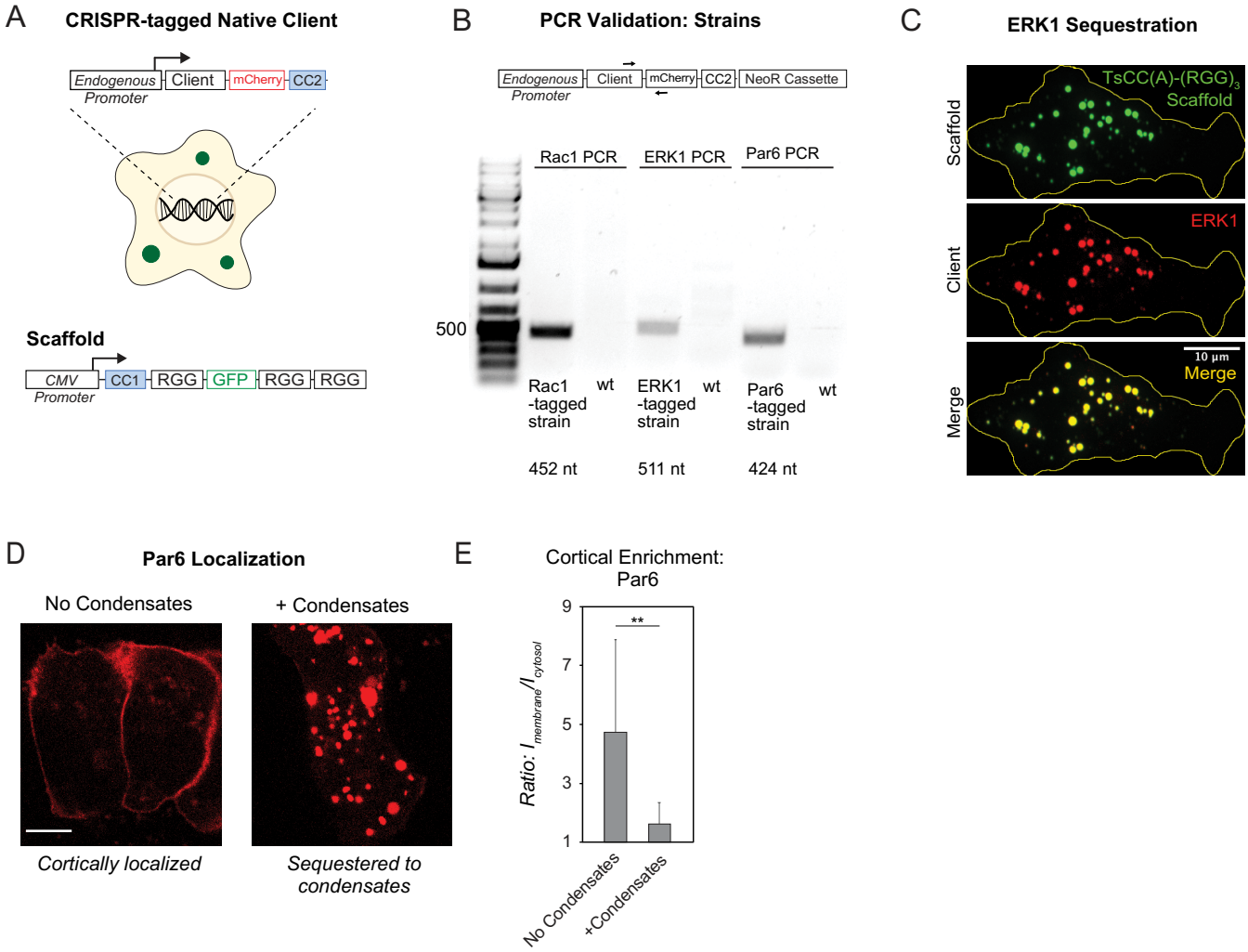

Extended Data Fig. 4 | Sequestration to synthetic condensates in mammalian cells. a, Schematic of CRISPR tagging approach to endogenous loci in mammalian cells and expression of the scaffold by a CMV promoter. **b**, PCR validation of CRISPR tagging in mammalian cell lines. Only tagged strains show a PCR product of the expected size as indicated. **c**, Representative images of tagged ERK1 robustly partitions to synthetic condensates formed by expression of TsCC(A)-$(RGG)_3$ scaffold. **d**, Representative images of tagged Par6 localized to the cell cortex in the absence of scaffold expression (left) and to condensate structures when scaffold is expressed (right). **e**, Quantitation of cortical Par6-mCherry-TsCC(B) in the absence and presence of condensates with cognate coiled coil. n = 10 cells for each condition. Error bars, s.d. Significance calculated by unpaired, two-tailed t-test. (**, $p < 0.01$).

nature research

Corresponding author(s): Matthew C. Good

Last updated by author(s): Jun 14, 2021

Reporting Summary

Nature Research wishes to improve the reproducibility of the work that we publish. This form provides structure for consistency and transparency in reporting. For further information on Nature Research policies, see our Editorial Policies and the Editorial Policy Checklist.

Statistics

For all statistical analyses, confirm that the following items are present in the figure legend, table legend, main text, or Methods section.

n/a	Confirmed	
☐	☒	The exact sample size (*n*) for each experimental group/condition, given as a discrete number and unit of measurement
☐	☒	A statement on whether measurements were taken from distinct samples or whether the same sample was measured repeatedly
☐	☒	The statistical test(s) used AND whether they are one- or two-sided *Only common tests should be described solely by name; describe more complex techniques in the Methods section.*
☒	☐	A description of all covariates tested
☒	☐	A description of any assumptions or corrections, such as tests of normality and adjustment for multiple comparisons
☐	☒	A full description of the statistical parameters including central tendency (e.g. means) or other basic estimates (e.g. regression coefficient) AND variation (e.g. standard deviation) or associated estimates of uncertainty (e.g. confidence intervals)
☐	☒	For null hypothesis testing, the test statistic (e.g. *F*, *t*, *r*) with confidence intervals, effect sizes, degrees of freedom and *P* value noted *Give P values as exact values whenever suitable.*
☒	☐	For Bayesian analysis, information on the choice of priors and Markov chain Monte Carlo settings
☒	☐	For hierarchical and complex designs, identification of the appropriate level for tests and full reporting of outcomes
☒	☐	Estimates of effect sizes (e.g. Cohen's *d*, Pearson's *r*), indicating how they were calculated

Our web collection on statistics for biologists contains articles on many of the points above.

Software and code

Policy information about availability of computer code

Data collection	Microscopy data was collected on an inverted spinning disk microscope under the control of Metamorph software.
Data analysis	Data was analyzed in ImageJ software and GraphPad Prism 9.

For manuscripts utilizing custom algorithms or software that are central to the research but not yet described in published literature, software must be made available to editors and reviewers. We strongly encourage code deposition in a community repository (e.g. GitHub). See the Nature Research guidelines for submitting code & software for further information.

Data

Policy information about availability of data

All manuscripts must include a data availability statement. This statement should provide the following information, where applicable:

- Accession codes, unique identifiers, or web links for publicly available datasets
- A list of figures that have associated raw data
- A description of any restrictions on data availability

Data supporting the findings of this study are included in the paper and supplemental materials. Original data is available upon reasonable request.

Field-specific reporting

Please select the one below that is the best fit for your research. If you are not sure, read the appropriate sections before making your selection.

☒ Life sciences ☐ Behavioural & social sciences ☐ Ecological, evolutionary & environmental sciences

For a reference copy of the document with all sections, see nature.com/documents/nr-reporting-summary-flat.pdf

Life sciences study design

All studies must disclose on these points even when the disclosure is negative.

Sample size	For in vivo yeast experiments, at least 50 cells were analyzed with few exceptions as noted in figure legends. For most mammlian experiments, at least 60 cells were analyzed. No statistical method was used to determine sample sizes a priori. This is a standard practice in this field.
Data exclusions	No data was excluded.
Replication	Experiments were reproducible.
Randomization	In all replicates for yeast experiments, identical cell lines were used in scaffold induced or uninduced conditions. In mammalian cell experiments, the same polyclonal population was transfected with a plasmid expressing the scaffold. Randomization was not possible.
Blinding	n/a. The presence of fluorophores marking the different localizations of endogenous proteins identifies the cell line and conditions. Most image analyses were performed using automatic scripts in ImageJ and do not require blinding.

Reporting for specific materials, systems and methods

We require information from authors about some types of materials, experimental systems and methods used in many studies. Here, indicate whether each material, system or method listed is relevant to your study. If you are not sure if a list item applies to your research, read the appropriate section before selecting a response.

Materials & experimental systems

n/a	Involved in the study
☒	☐ Antibodies
☐	☒ Eukaryotic cell lines
☒	☐ Palaeontology and archaeology
☒	☐ Animals and other organisms
☒	☐ Human research participants
☒	☐ Clinical data
☒	☐ Dual use research of concern

Methods

n/a	Involved in the study
☒	☐ ChIP-seq
☒	☐ Flow cytometry
☒	☐ MRI-based neuroimaging

Eukaryotic cell lines

Policy information about cell lines

Cell line source(s)	Yeast cells of the YEF473 genetic background were a gift from Erfei Bi. The tor1-1 fprΔ strain used for rapamycin-mediated recruitment of clients to in vivo condensates are in the BY4741 yeast genetic background and was a gift from Anuj Kumar. Both genetic backgrounds are standard lines in yeast research. For mammalian cell culture, U2OS osteosarcoma cells from ATCC were used.
Authentication	All cell lines were authenticated by PCR on genomic DNA to confirm integration followed by screening for appropriate fluorophore signals and localization. U2OS cell lines were obtained from ATCC and certified mycoplasma free. No authentication was performed beyond confirming genomic integrations.
Mycoplasma contamination	Cell lines tested negative for mycoplasma contamination.
Commonly misidentified lines (See ICLAC register)	No commonly misidentified lines were used.